POLITECNICO
MILANO 1863

SCUOLA DI INGEGNERIA INDUSTRIALE
E DELL'INFORMAZIONE

Implantable microelectronic system for dopamine sensing using microwire-based electrodes

Tesi di Laurea Magistrale in
Electronics Engineering - Ingegneria Elettronica

Author: **Ali Meimandi**

Student ID: 926372
Advisor: Prof. Marco Carminati
Co-advisors: Sandro Carrara, Timothy G. Constandinou
Academic Year: 2021-22

Abstract

Since the discovery of the electrical signal in the body of living beings, scientists have been curious to find the mysterious applications behind these signals. Nervous system is the most important network in the body which is utilizing the electrical signals to transfer the data across the body. The Neural measurement and stimulation is one of the most impactful means for discovering the functions of the brain as the core of the nervous system. Sensing the chemical reactions inside the brain plays a majority of roles in providing information regarding the progress of some neurological disorders. To achieve this aim, Brain-Machine Interfaces (BMIs) provide the opportunity to go deep through the brain neurons and provide information about electrochemical reactions. It has been discovered that neurotransmitters play a special role in the functioning of glial cells in the brain and, therefore, new needs for measuring them in situ emerged in neuroscience.

Measuring neurotransmitters concentration, such as dopamine, facilitates the approach toward the restoration of movements and reliable social communications in patients (e.g., in autism). Dopamine (DA) dysregulation and deficiency also cause debilitating movement and mood disorders such as addiction, depression, Parkinson's disease, and schizophrenia.

This project presents an experimental methodology to enable dopamine concentration measurements in-vivo by using ultra-micro electrodes with a full-custom designed microelectronic sensor.

An experimental setup has been designed for further investigation regarding the integration of a dopamine sensor in an implantable system by using the designed CMOS potentiostat. This setup is able to measure the range of dopamine concentration from 0.3 μM to 2 μM, which entirely covers the possibility of dopamine concentration ranges in the human brain. A 3-electrodes configuration has been designed and tested experimentally to monitor dopamine in different concentrations by using the electrochemical method named Fast Scan Cyclic Voltammetry (FSCV). Microwires are of 25 μm in diameter to reduce the capacitive current.

In addition, An integrated CMOS potentiostat has been designed using Cadence® Virtuoso as well, in order to measure dopamine concentration in future in-vivo experiments.

The plan here is to integrate this potentiostat into the ENGINI platform to wirelessly monitor the dopamine concentration in-vivo. Post-Layout simulations show that the potentiostat eliminates the background current and measure the faradic current produced by the dopamine redox reaction.

Keywords: Neural Dust, CMOS, Integrated Circuit, Neurotransmitter, Dopamine, Microelectrode, Electrochemical Sensing, Fast-Scan Cyclic Voltammetry

Contents

Abstract **i**

Contents **iii**

1 Introduction **1**
1.1 ENGINI Platform . . . 3
1.1.1 ENGINI probe architecture . . . 5
1.2 Dopamine from neuroscience point of view . . . 6
1.3 Concentration of Dopamine inside the brain . . . 8

2 Dopamine electrochemical measurement **11**
2.1 Electrochemical techniques and Cyclic Voltammetry . . . 11
2.2 Electrodes characteristics . . . 15
2.3 Experimental setup and materials . . . 17
2.4 Sensor Calibration . . . 20

3 Electronic Design for Dopamine Measurement **23**
3.1 Cadence Virtuoso . . . 23
3.1.1 Schematic design . . . 23
3.1.2 Layout design . . . 24
3.2 IC design . . . 25
3.2.1 Current sources . . . 27
3.2.2 Folded-Cascode OTA . . . 32
3.2.3 Comparator . . . 34
3.3 Test Board Design . . . 40
3.3.1 IC packaging . . . 40
3.3.2 Board design . . . 41

4 Results **45**

4.1 Circuit simulation results 45
4.1.1 5 bits controlled current source 45
4.1.2 Folded cascode OTA 47
4.1.3 Comparator 48
4.1.4 System level results 49
4.2 Electrochemical results 52

5 Conclusions and future developments **59**

Bibliography **61**

A Appendix A **67**

List of Figures **71**

List of Tables **75**

Acknowledgements **77**

1 | Introduction

Neural engineering is an interdisciplinary research area that uses novel methods from neuroscience and engineering to understand, repair, replace, enhance or exploit the properties of neural systems[30]. The initial step toward this objective was to understand the brain better in terms of anatomy and physiology. The electrical current was first observed by M.D. Richard Caton of Liverpool, the UK, in 1875. It was the starting point for discovering the mysterious functions of the brain [13].

Thanks to the advancements in Medical sciences and Engineering fields, researchers are interested in monitor and stimulating the different applications of the brain to restore neural disabilities. Brain-computer interfaces(BCIs) were introduced as neuroprostheses and are meant to create the links between the Central Nervous System and the outside world. BCIs can extract features from recorded signals and translate them into artificial outputs that act either on assistive technologies or on the body, bypassing the biological lesion [12].

There are two different methodologies for BCIs: Open-loop and Closed-loop. In open-loop architecture, the purpose is to monitor the functionality of the nervous system and derive different features. While in closed-loop architecture, In addition to the open-loop features, the stimulation of sensory pathways in the CNS to better guide artificial motion is considered.

In recent years, a new paradigm, smart dust, came into play. This term was discussed for the first time at a conference in 1999. The application of smart dust to monitor biological systems came from two exciting branches, which are 1)brain monitoring and stimulation and 2)metabolism monitoring[10]. In 2013 Jan M. Rabaey and Michel Maharbiz in UC Berkeley published a conceptual paper in the ArXiv proposing a new “Neural Dust” application for brain monitoring. A few years later, this article was followed by another conceptual paper in the same ArXiv, by Sandro Carrara and Pantelis Georgiou, who expanded to a new application called “Body Dust” for the telemetry of human metabolic conditions[11].

One recent research carried out on neural dust is the Empowering Next Generation Implantable Neural Interface (ENGINI) platform. Laboratory of Next Generation of Neural

Interfaces (NGNI), which is attached to the Centre of Bio-Inspired Systems (CBIT) within the Institute of Biomedical Engineering at Imperial College London (ICL), is conducting this project to 1) develop a smaller, more superficial, well-engineered probe and 2) deploy multiple devices across the brain. (Figure 1.1)

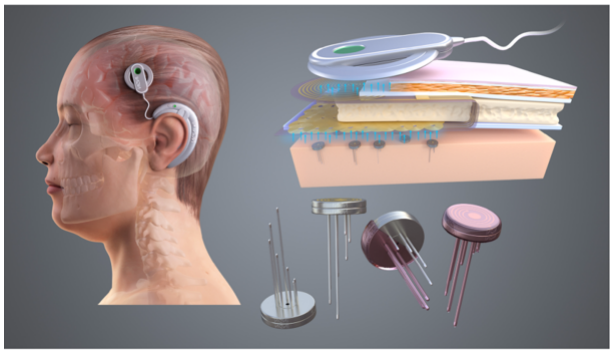

(a) ENGINI System: power supply,transceiver and probes.

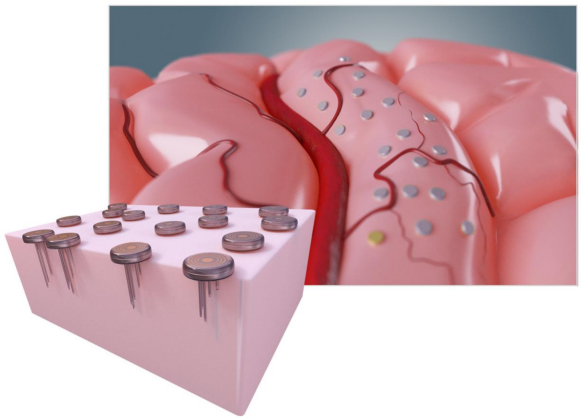

(b) NGNI probes Distributed across the cerebral cortex.

Figure 1.1: Overview of the ENGINI system

In this platform, a bidirectional communication system is proposed to send the data from the probes to the outer part and to receive power from external transmitters to the probes. The external circuitry should send power to the internal system, and the internal system should provide energy to power the electronic parts. Then the information will be sent back wirelessly to the external base. The data are processed in the external part, and the needed information will be extracted[2].

1.1. ENGINI Platform

Empowering Next Generation Implantable Neural Interface (ENGINI) platform is one of the Brain Machine Interfaces (BMI) which is following the trend of achieving scalibility by employing a distributed organization of multiple (10s to 1000s), miniature (mm or sub-mm scale) devices that can work completely wireless and operate independently of one another. Wireless power transfer can be facilitated by electromagnetic or ultrasonic transmission with data encoded in the carrier (downlink) and through backscatter (uplink) The power and data transmission scheme has been shown in Fig. 1.2.

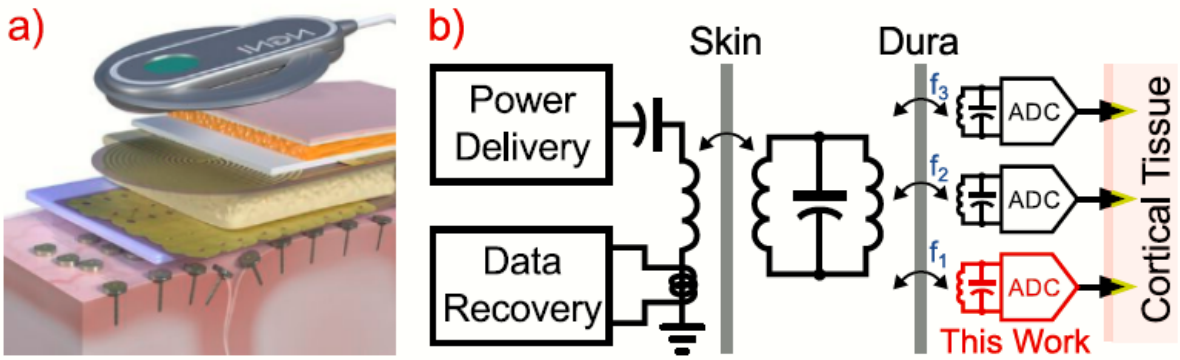

Figure 1.2: The ENGINI concept showing: (a) multiple freely floating probes being wirelessly interrogated by a headstage unit; (b) schematic representation. Reprinted from [25]

The ENGINI platform consists of 3-tier network for realization of a distributed architecture:

1. mm-scale sub-dural intracortical recording implants
2. customized cranioplasty with embedded transponder
3. external head-based 'processor' with battery

This structure has been shown in Fig 1.3. This 3-tier structure improves the power transfer efficiency by partitioning the linkage between external part and implants into cm-scale transcutaneous link and multiple mm-scale transdural links. Good uniformity in power distribution has been achieved by overlapping of the mm-scale coils on the subcranial primary[15].

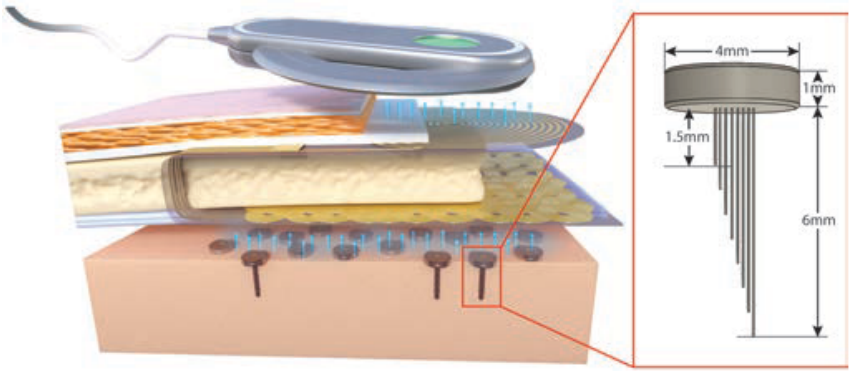

Figure 1.3: ENGINI platform concept showing 3-tier link for wireless power/data transfer and a sample probe with eight channels. Reprinted from [1]

As shown in Fig 1.3, 8 microwires has been considered for the ENGINI platform to reach the maximum stability in recordings and observe field potentials in different depths.[34] In this platform the microwires has been designed to have lengths between 1.5 mm and 6.0 mm. Each probe takes advantage from locallly-referencing recordings that has the benefit of common-mode noise rejection and increasing the spatial focus of the LFPs.[2] The external processor is responsible for the informative features from the differential LFPs. These features can be extracted form the time domain[16, 17, 36] and frequency domain[16, 36, 43]. In the next step the data should be directly decoded or the features should be used for inferring the underlying spikes dynamics. This is achieved by employing the deep learning techniques which is deployed in a small, portable and low power platform[3].

1.1.1. ENGINI probe architecture

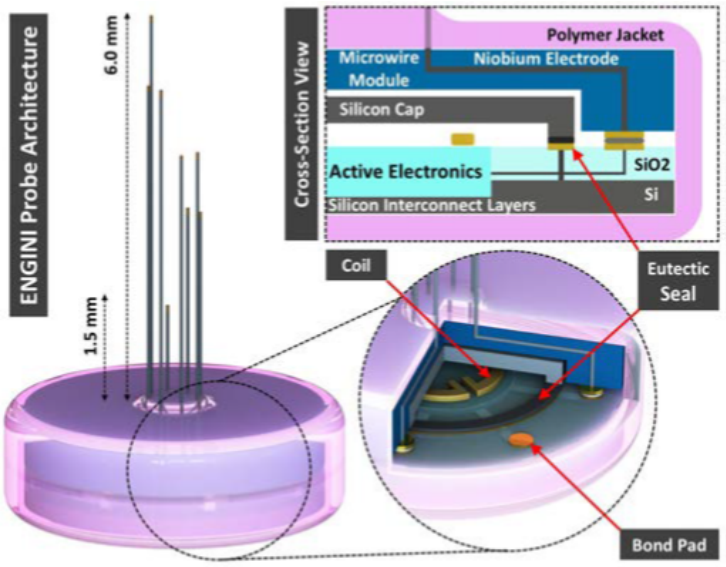

Figure 1.4: ENGINI probe construction and packaging concept, combining two subsystems: (1) hermetically-packaged microelectronic module; (2) polymer-encapsulated microwire array. Illustration not to scale. Reprinted from [2]

Each probe contains a fully integrated wireless power and data transmission which is able to manage the power, amplify the signal and perform data telemetry. A coil inside the probe harvests the power at 433MHz frequency. A control block can regulate the power of the system by digitally tuning the impedance of the resonant tank. The figure of control block is shown in Fig 1.5.

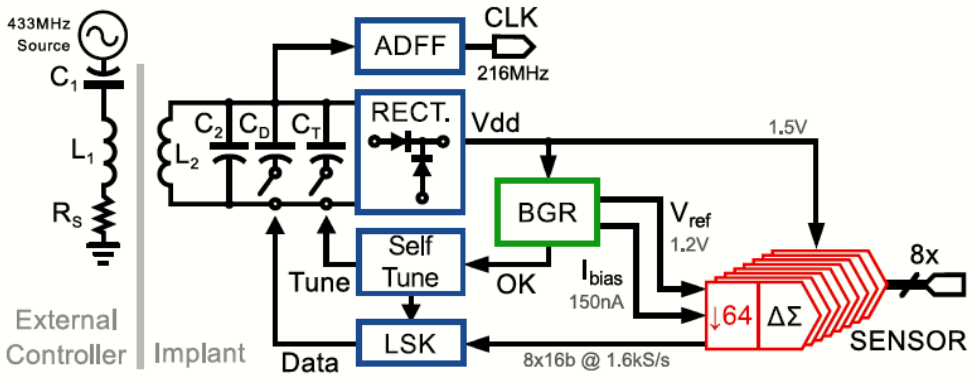

Figure 1.5: ENGINI probe architecture for recording LFP at high resolution from 8 electrodes. The system tunes resonant tank L2C2 to regulate VDD. Reprinted from [25]

The sensor uses multiple oversampling data converter to digitize the electrode recordings with high power efficiency.
The probe of the ENGINI platform is manufactured using the biocompatible materials and they are compatible with CMOS within an acceptable temperature range.
Each probe consists of two sub-sections that are interconnected:
(1) The micropackaged active silicon head
(2) Passive interposer that houses the microwire electrode array
The micropackaged active silicon head is composed of two silicon substrates connected to each other by a seal of gold eutectic which is a barrier against the moisture to enter into active electronic part.[26] Gold-tin ensures CMOS compatibility, corrosion resistivity and long-term reliability.[38] The two substrate houses: (1) The CMOS chip which includes the ENGINI recording system, coil and planar contact for interconnection of micro wires.[39] (2) a silicon cap to form a gas-filled cavity.
The microwire array is moulded into the passive interposer structure that provides good mechanical stability for the system. All the system is surrounded by a polymer jacket.

In this project we are going to design a potentiostat that can be embedded in the active silicon head of the ENGINI probe and it is able to measure the dopamine concentration in-vivo. In addition an investigation on the micro-electrodes which are suitable for dopamine measurement has been done. In the end, the compatibility of the electrochemical results with performance of the designed potentiostat has been evaluated.

1.2. Dopamine from neuroscience point of view

For electrochemical detection of the neurotransmitters, they can be divided into three main groups. the first group is electrochemically active compounds likes epinphrine, norepinephrine and tyrosine derivatives dopamine. Many of their metabolites such as 3,4 dihydroxyphenylacetic acid(DOPAC) and I-dopa are also active. All of these compounds can be detected by electrochemical reaction of the molecule. In addition, Other substances like uric acid, nitric acid, ascorbic acid, oxygen or hydrogen peroxide are detectable by electrochemical methods.
The second group of neurotransmitters is not essentially electroactive so these compounds can not be detected by traditional electro-analytical methods. But, they can be oxidized by an enzymatic reaction. these reaction can be monitored by corresponding the enzyme reaction with an electrochemical reaction. some important transmitters in this group are glutamate and GABA. Glucose and lactate which play rolls in energy production in the

brain can also be detected with this indirect method.
Neuroactive peptides and some amino acid neurotransmitters create the third group of neurotransmitters which are not directly detectable using electrochemical biosensors. But, neuropetides with electrochemically active group can be detected.[18]

Dopamine is one of the neurotransmitters of the first group. Dopamine is an important metabolite present in our brain. It is a neurotransmitter that enables the communication between neurons. It is a hormone packaged in the vesicle of neurons.
Dopamine is formed by the decarboxylation of l-DOPA. The redox reaction of dopamine has been shown in Fig. 1.6.

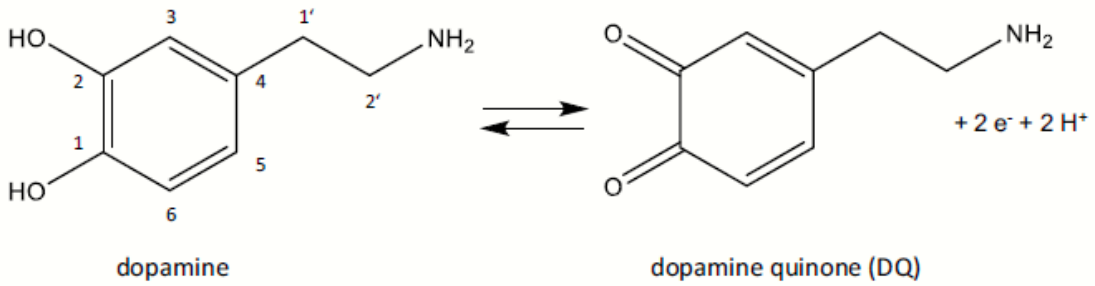

Figure 1.6: Structure of 4-(2-aminoethyl)benzene-1,2-diol (IUPAC name for dopamine) and oxidation to Dopamine Quinone (DQ) in a 2-electron oxidation. Reprinted from [32]

When a presynaptic stimulus arrives at a neuron, the vesicle releases dopamine into the synapse. The released dopamine activates dopamine receptors that are spread throughout the brain. Thus, dopamine has a vital role in the metabolic system because it is involved in several neurological processes, for instance, motivation, pleasure, cognition, learning, memory, and motor control[22]. It is also released into the blood to support endocrine signaling (the system of releasing hormones directly into the bloodstream to control and regulate the body). Therefore, dopamine molecules are also used for pharmaceutical purposes because they affect the sympathetic nervous system in regulating the heart rate, blood pressure, and other essential functions. Furthermore, it is used in intravenous medications to treat cardiovascular diseases.[9]

1.3. Concentration of Dopamine inside the brain

The level of extracellular dopamine is modulated by two mechanisms in the brain: phasic and tonic activity. Phasic dopamine release, like most neurotransmitter releases in the nervous system, is driven directly by action potentials in the dopamine-containing cells. Tonic dopamine transmission occurs when small amounts of dopamine are released without being preceded by presynaptic action potentials. Tonic transmission is regulated by various factors, including the activity of other neurons and neurotransmitter reuptake. In the striatum, shown in Figure 1.7, these tonic transmissions are estimated to result in 5-20 nM of dopamine. However, the extracellular dopamine concentration is increased up to $>$ 1000 nM for a short time when the phasic activity is present.[23, 37]
It has been shown previously that dopamine transients are on the order of 50 - 100 nM in rats and reach values higher than 200 nM with the use of drugs. In awake monkeys with electrical stimulation, dopamine transients reached 850 nM dopamine while it can reach to 2 μM in human brain[20, 31, 33]

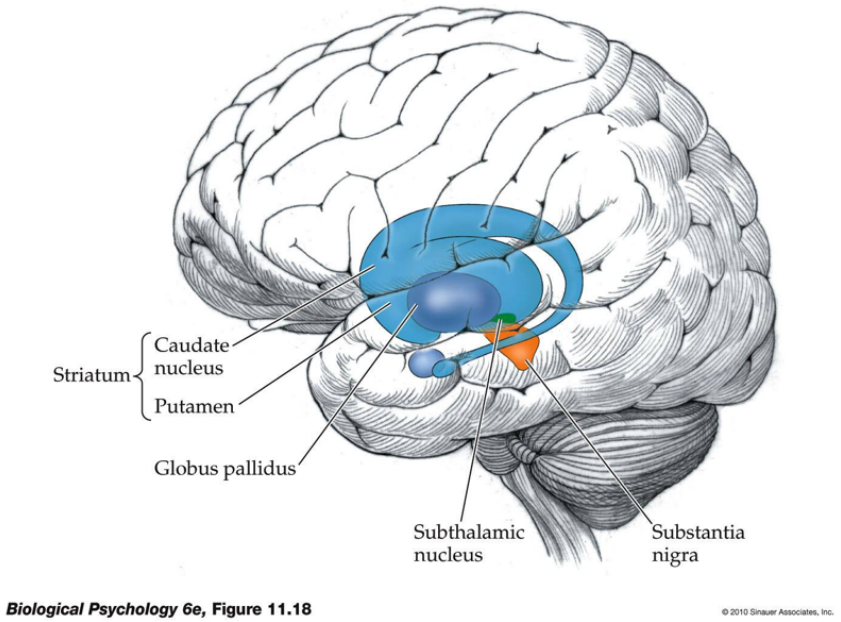

Figure 1.7: Potential places for measuring the dopamine concentration

An experiment that has been done on Parkinson's patients and healthy humans shows that the change in dopamine concentration in Parkinson's patients is significant. The results are summarized in Figure 1.8. In control subjects, dopamine concentrations were similar in the putamen, caudate nucleus, and nucleus accumbens. In the substantia nigra,

they were 5 - 10 times lower in the pars reticulata than in the pars compacta. In Parkinsonian and supranuclear palsy patients, dopamine concentrations were significantly lower than controls in all the studied structures. In the dopamine terminal regions, the most significant decrease was observed in the putamen, followed by the caudate nucleus and the nucleus accumbens. In the substantia nigra the decrease in dopamine concentrations was more significant in the pars reticulata.[7]

Dopamine, HVA and HVA/DA ratio in the nigrostriatal and mesolimbic dopamine systems in subjects with Parkinson's disease and supranuclear palsy. Values represent the mean with S.E.M. expressed as ng/g tissue.

	Control	Parkinson	Supranuclear palsy
Putamen			
DA	2506 ± 398	84 ± 10 (−97%) [a]	191 ± 64 (−92%) [a]
HVA	5182 ± 553	1780 ± 268 (−66%) [a]	2530 ± 870 (−51%) [a]
HVA/DA	2.84 ± 0.58	19.26 ± 3.01 (678%) [a]	14.20 ± 3.34 (500%) [a]
Caudate nucleus			
DA	2428 ± 479	353 ± 53 (−85%) [ad]	457 ± 60 (−81%) [a]
HVA	3956 ± 379 [c]	1796 ± 225 (−55%) [a]	2312 ± 538 (−42%) [a]
HVA/DA	2.52 ± 0.44	7.24 ± 1.14 (287%) [a]	5.28 ± 1.13 (210%) [a]
Nucleus accumbens			
DA	2130 ± 197	672 ± 196 (−68%) [ac]	
HVA	5665 ± 1131	4138 ± 877 (−27%)	
HVA/DA	2.59 ± 0.26	5.21 ± 0.57 (201%) [a]	
S. nigra compacta			
DA	465 ± 75	103 ± 20 (−78%) [a]	
HVA	3576 ± 419	2193 ± 358 (−39%) [a]	
HVA/DA	8.14 ± 0.75	22.20 ± 0.28 (258%) [a]	
S. nigra reticulata			
DA	209 ± 29 [b]	< 15 (> −93%) [a]	
HVA	2218 ± 209 [b]	1720 ± 117 (−22%) [a]	
HVA/DA	11.61 ± 1.28 [b]	> 202 (1740%) [a]	

[a] All values are significantly different from controls, $P < 0.02$, except for HVA concentrations in the nucleus accumbens. [b] Significantly different from pars compacta of controls, $P < 0.02$. [c] Significantly different from putamen and nucleus accumbens of controls, $P < 0.05$. [d] Significantly different from putamen and nucleus accumbens of Parkinsonians, $P < 0.001$. [e] Significantly different from putamen and caudate nucleus of Parkinsonians, $P < 0.001$.

Figure 1.8: Compare of Dopamine concentration between Parkinson's patients and control group in different regions of brain. Reprinted from [7]

It is often used to record DA concentration in the striatum, where norepinephrine (electrochemically indistinguishable from DA) is in sufficiently low concentrations so as to not interfere with DA measurements. [33]

Characterizing and providing real-time measurements of rapidly fluctuating dopamine in vivo requires an analytical method with rapid temporal resolution. The next chapter will describe a specific electrochemical method called cyclic voltammetry by referring to certain parameters of this method.

2 | Dopamine electrochemical measurement

2.1. Electrochemical techniques and Cyclic Voltammetry

Detection of neurotransmitters in the first group is done using different electrochemical methods. The most used methods are chronoamperometry, constant potential amperometry, cyclic voltammetry and fast-scan cyclic voltammetry.
In constant potential amperometry the working electrode is kept at a DC constant potential which is sufficient for oxidation or reduction of the desired compound. Due to the existence of the compound and its reaction a current of electrons is flew in the electrode. The integral of this time with respect to time gives the transferred charge that is proportional to the concentration of the species electrolyzed at the electrode surface.[27]
With this method a very high time resolution can be achieved. With a sampling rate in the kHz range this method can monitor signals on the submillisecond time scale. It should be taken into account that constant potential amperometry is a non-selective method. All the electroactive species which oxidize or reduce in this potential can generate the faradaic current. Therefore, it is necessary to identify the amount of the current produced by the desired compound.
A sample graph of constant potential amperometry has been shown in Fig 2.1.

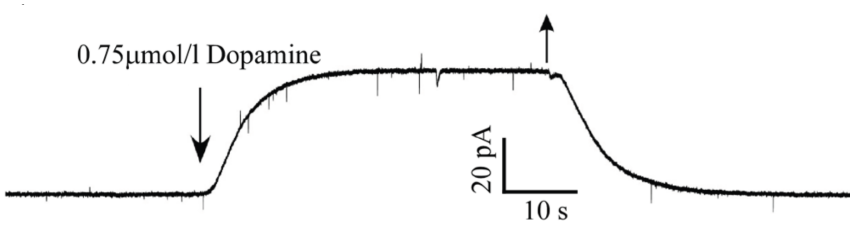

Figure 2.1: A representative constant potential amperometric response of a 100 μm long carbon tip to 0.75 $\mu mol/l$ dopamine at 0.65V in a miniature perfusion chamber. Reprinted from [8]

In chronoamperometry the potential is immediately stepped from a potential, which no electrochemical reaction is occurring, to a potential which is sufficient for the oxidation and reduction of the desired compound. Then the potential is immediately steps back to the initial voltage. The current measured at a fixed time into the potential step is proportional to the concentration of the analyte. When the potential comes back to the initial value the species that were oxidized will be reduced.[24] Chronoamperometry has a greater selectivity than constant potential amperometry. It has been used to measure dopamine[28, 40] and serotonin[14, 29] concentration in the extracellular fluid of the brain. Fig. 2.2 shows the concept of the chronoamperometry method.

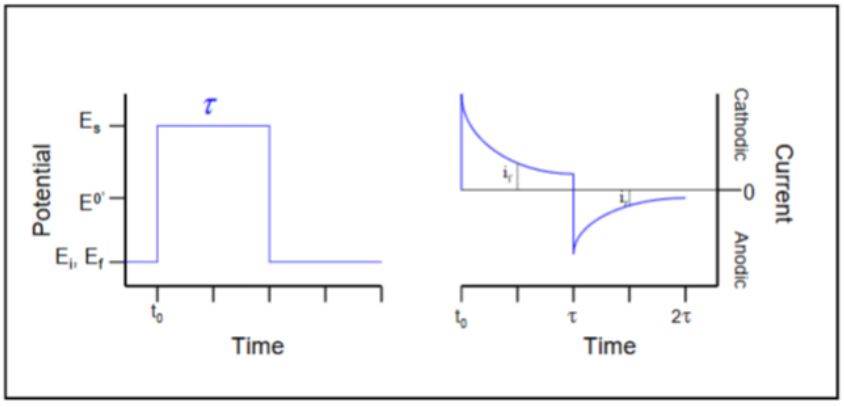

Figure 2.2: Double potential step chronoamperometry has been shown in this figure. On the left the applied potential is shown while on the right the response of the system to this potential is shown.

Cyclic voltammetry is one of the most popular electrochemical methods to measure various chemical compounds. A voltage scan toward positive and then negative potentials with the continuous acquisition of current is called cyclic voltammetry and is very useful for measuring the suitable potentials at which redox reactions occur. We can observe two

clear peaks related to the oxidation and reduction processes.
There are two different electrochemical measurement configurations: two-electrode configurations and three-electrode configurations.
In the two-electrode configuration, we use the reference electrode (RE) and working electrode (WE). By applying a sweeping voltage between the working electrode and the reference electrode, the current passing through the reference electrode and working electrode is measured. In the two-electrode configuration, the RE acts as an electron supplier by passing the current and as a potential reference for WE by keeping its potential constant. Due to a varying current passing through, keeping a constant voltage across the cell is hard.[21]
In a three-electrode configuration, an auxiliary electrode in addition to these two electrodes will be used. The varying voltage with respect to the time is applied between the working electrode and reference electrode, and the current occurring on the working electrode is passed through the working electrode and counter electrode so the reference electrode can preserve a stable voltage. The counter electrode chosen from inert materials does not contribute to the reaction happening inside the cell. Also, the counter electrode should have a larger surface area with respect to the working electrode to not limit the current of the working electrode.
When the potential goes toward the negative values, the electrons' energy increases to higher levels, which is transferred to the electrolyte. As a result, a current goes from the solution to the electrode, called reduction current. When the electrode potential goes to positive values, electrons move from the electrolyte to the electrode, and the current is produced from electrode to solution, called oxidation current.
The current measured using the working electrode consists of two different components. The first one is the faradaic current resulting from the redox reaction dopamine. The second contribution, called capacitive current, comes from the absorption and desorption of ions at the electrode/electrolyte interface. This phenomenon can be modeled as an electrical double layer capacitor whose value is variable by changing the voltage.
The controlling potential applied across the working and reference electrodes can be considered an excitation signal. This excitation signal can sweep in the forward and reverse scans between two upper and lower voltages, called switching voltages. The oxidation and reduction peak voltages should be in the range of switching voltages. The sweep has a staircase shape; the voltage is changed by specific step voltage, and the current is measured at each step.
The peak currents, measured at oxidation and reduction voltages, are proportional to the concentration of the compound and follow the Randles-Sevcik formula[4].

Randles-Sevcik equation:

$$i_p = 0.4463 \times nFAC \times \sqrt{\frac{nFvD}{RT}} \tag{2.1}$$

In this equation, n is the number of electrons exchanged, v is the scan rate used for the potential sweep (V/s), F is Faraday's constant, A is the active area of the working electrode (cm^2), R is the gas constant, T is the absolute temperature (K), D is the diffusion coefficient of the analyte (cm^2/s).
The voltammogram is the plot of current vs. voltage from the experiment, and it can have multiple peaks depending on the number of electrolytic processes taking place in the electrochemical system.
In order to reach the faradaic current from the cyclic voltammetry, the background current(capacitive current) should be subtracted from the cyclic voltammogram. The capacitive current can be subtracted by measuring the baseline current of the cell before starting the measurement of compound concentration. Another possible way is to calculate the faradaic current by calculating vertically from the extrapolated steady-state graph, as shown in Fig 2.3

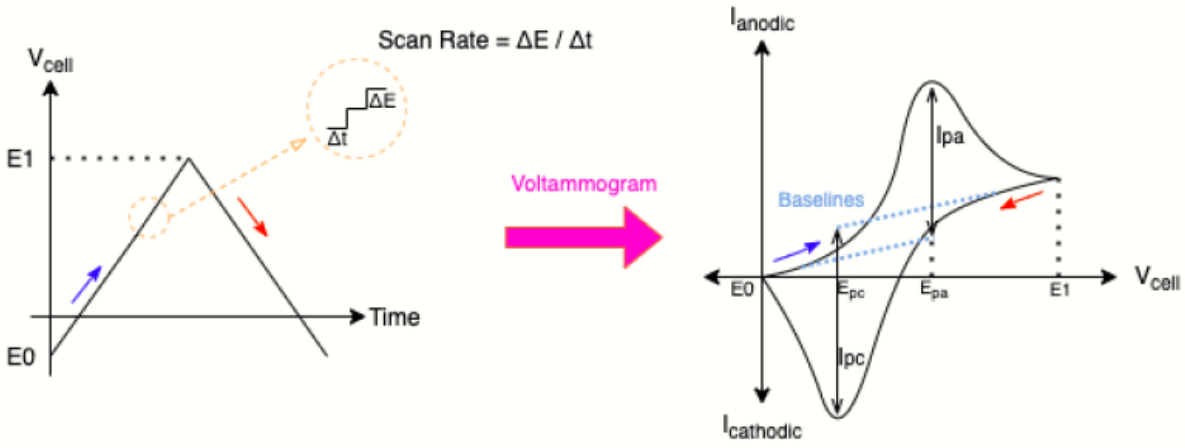

Figure 2.3: Two linear potential scans are applied to the electrochemical cell while measuring the resulting current: Forward scan (blue) and reverse scan (red). Voltammogram is the graph plotting Current vs. Potential.

Voltage scan rate is an essential parameter in the measurements. To understand its effect, we should consider the two types of currents passed through the working electrode. i_c is the charging current that comes from the capacitive effect of the electrical double layer. The capacitive current is proportional to the scan rate(v) , which can be calculated from

the formula below.

$$|i_c| = AC_d v \tag{2.2}$$

where A is the active area of the sensing electrode, C_d is the double layer capacitance, and v is the scan rate. i_p is the faradaic current that comes from the Randles formula given in Formula 2.1. The ratio between capacitive and faradaic current shows that this ratio increases by increasing the scan rate, and the capacitive current can mask the faradaic current by increasing the scan rate.
To measure the low concentration of dopamine, Fast Scan Cyclic Voltammetry (FSCV) is the most common method to have a high sensitivity and low Limit of Detection (LoD). Background-subtracted FSCV is a powerful tool for making real-time, subsecond measurements of electroactive molecules in discrete brain regions. This approach has been used by Millar and colleagues and has been increasingly used in the past decade due to technological improvements made by Wightman and colleagues.
In order to limit the effect of capacitive current in FSCV, using ultra-micro electrodes is desired. The critical value defined for ultra-micro electrodes is 25 μm. The microwires used in our experiments are 25 μm in diameter. Their small size is necessary for increasing the scan rate range for cyclic voltammetry experiments since the resistance of the electrode is proportional to the area of the electrode, and smaller resistance values allow us to have a reasonable time constant that determines the time required for the current to rise to the level where the faradaic process starts. Increased charging currents with the increased scan rate limit the useful area range of the electrode. With UMEs, one can increase the scan rate up to 10^6 V/s.[6] Furthermore, using fast-scan cyclic voltammetry and ultra-micro electrodes are desirable since the probes will be implanted in the striatum of the human brain, and they should cause the minimum tissue damage and can be able to take measurements in short time scales.

2.2. Electrodes characteristics

The electrochemical measurement is done using three electrodes configuration, which show the more accurate current measurements. The function of each electrode is described below [9]:

1. A working electrode that contains all the structures required to make the redox system work in an efficient manner.

2. A reference electrode that supplies the right potential to get the right redox.

3. A counter electrode to get the measurement of the current from the redox.

The structure of the three electrode configuration has been shown in Fig 2.4.

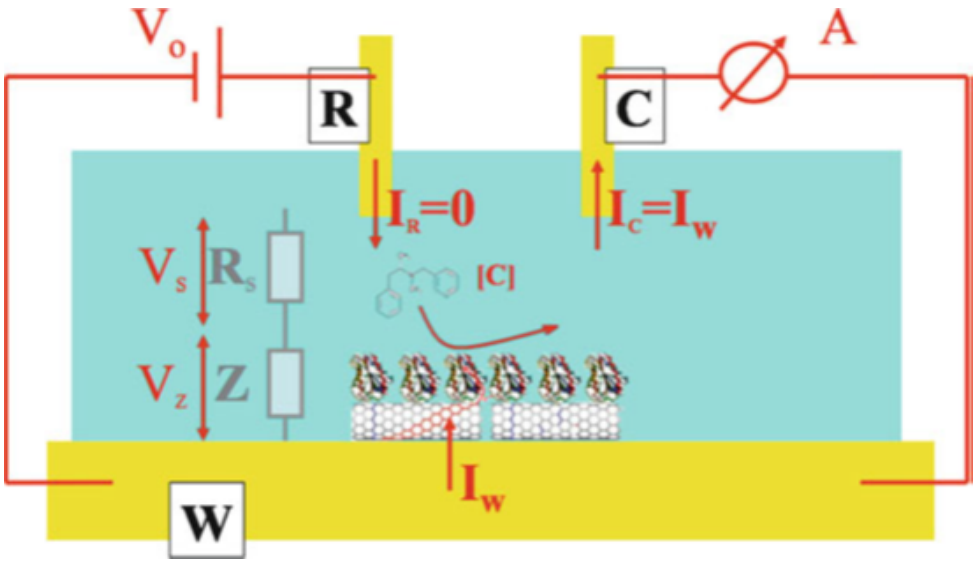

Figure 2.4: Three-electrode electrochemical cell with nano/bio structures. Reprinted from [9]

In order to select the type of the electrodes, some considerations should be evaluated.
The Reference electrode should preserve a constant voltage in the cell so that the working electrode potential can be swapped accurately. The reference electrode is usually from Platinum or Ag/AgCl. The reference electrode of Platinum has been chosen for our experiments.
The counter electrode should be inert to not contribute to the electrochemical experiments being done in the electrochemical cell. Also, the surface area of the counter electrode should be larger than the working electrode not to limit the current passing through the working electrode. The counter electrode which has been chosen for dopamine measurement is from Platinum.
The working electrode plays a significant role in electrochemical measurement since the working electrode captures the redox reaction. The mechanical and electrical measurements of the electrodes for the ENGINI platform have been investigated in a research project.[2] Since the probes will be implanted inside the brain, they should provide an excellent mechanical functionality to not bend or break during implantation and small brain movements. Tungsten wire has been considered as the working electrode for the probe. Tungsten electrodes have higher rigidity with respect to Platinum and gold and carbon microelectrodes while it can be bent without ant damage. The rigidity of a material is

quantified by the tensile modulus, which can be calculated by equation 2.3. Tungsten wires are are sufficiently stiff to be used without any further support.

$$E = \frac{\sigma}{\epsilon} \tag{2.3}$$

In this equation σ is uniaxial force per unit surface and ϵ is proportional deformation (change in length divided by original length) and E is tensile modulus.

All the microelectrodes have been purchased from the Advent® research materials center.

2.3. Experimental setup and materials

Since the dopamine concentration inside the brain can reach up to 3 μM, measurement of dopamine concentration in this range has been done in our experiments. In vitro experiments have been done using Autolab® PGSTAT128N potentiostat. A relatively low scan rate of 50V/s was used in this experiment since high surface reactivity causes the background current to reach the current limit of the FSCV apparatus. in this experiment, the upper voltage for FSCV is 1.3V, and the lower voltage is -0.4V and each step of staircase cyclic voltammetry equal to 26mV is considered. The procedure of FSCV has been shown in Fig. 2.5

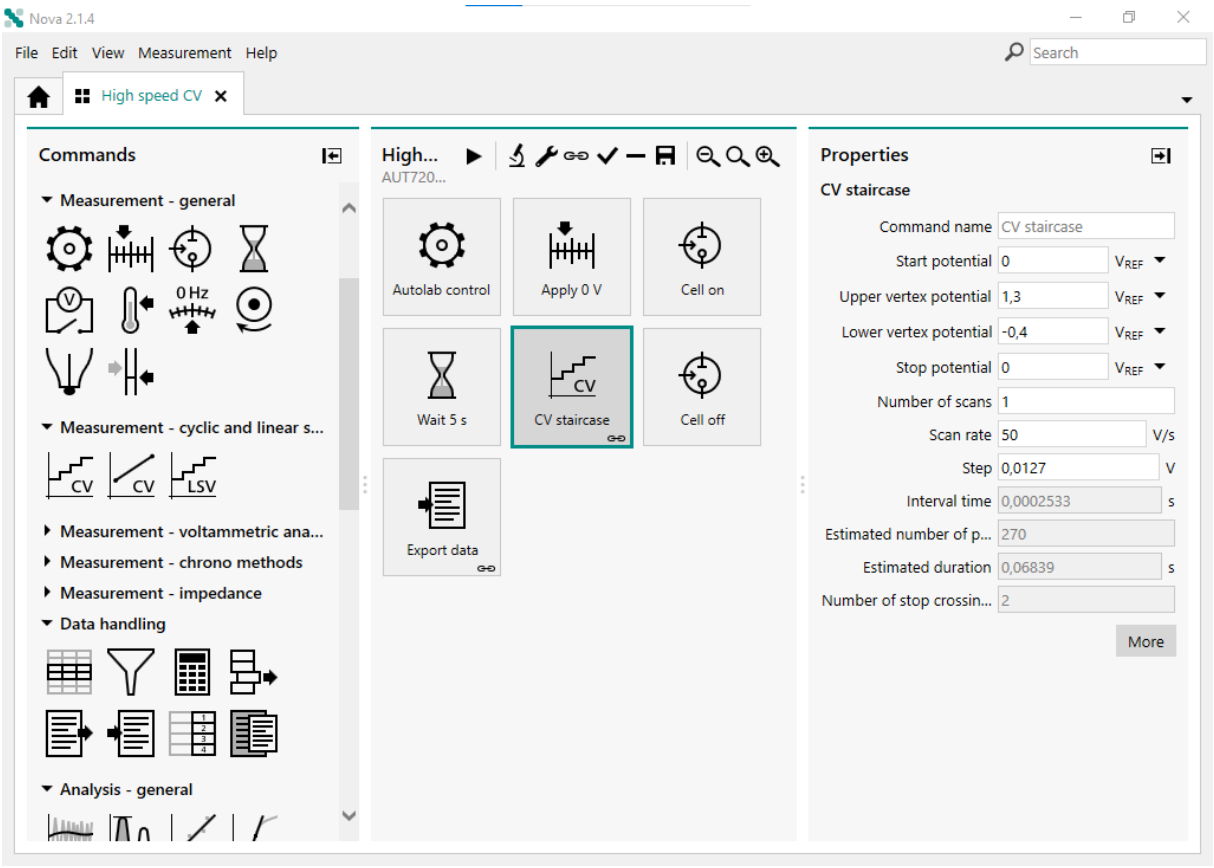

Figure 2.5: Fast-scan cyclic voltammetry procedure done using NOVA software for Dopamine measurement using the micro-electrodes.

The potentiostat is equipped with the NOVA® software for doing different measurements. There is a possibility to create the procedure manually or using the predefined procedures in the software. In Dopamine measurement the following procedure has been created:

1. The "Autolab control" module create a shortcut to the main setup of potentiostat. In this module the potentiostatic or galvanostatic mode of measurement is chosen. In the potentiostatic mode the configuration of procedure is based on the voltage while in the galvanostatic procedure the configuration is based on the current. Also the expected current range should be chosen to tune the device for removing the environmental noise.

2. A module for applying a DC voltage between the working electrode and reference electrode is used to stabilize the device before starting of the measurement.

3. The next module turns on the cell and zero voltage is applied to the solution.

4. A module has been put to create a delay of 5 seconds to stabilize the micro-electrodes

which are surrounded by the solution.

5. The main module in the analysis is "CV staircase" which is responsible for doing the cyclic voltammetry. In this module the potential which the CV is started is specified. Also the upper and lower and potential are defined. In this measurement start and stop potential are zero and the scanning is done between -0.4V and 1.3V . The scan rate is $50V/s$ and the steps that the device should sample the data is defined. Based on the limitation of the device 0.0127V was the smallest step that the ADC of potentiostat was able to work in this scan rate.

6. In the end of the CV measurement the cell of the potentiostat is turned of and the link between the device and micro-electrodes are disconnected.

7. To record the data measured in CV analysis the module of "Export data" has been used. In this module the number of columns and type of data are specified. This module should be linked to the "CV staircase" module to record the data of this module. It is done by Keeping "Ctrl" key of the keyboard and selecting the two module and pressing the link option.

In order to have an accurate faradaic current measurement, the background current was measured ten times to reach a stable background current, and the microelectrodes reached a stable conductivity in the solution.
To have a similar solution to the brain environment, Phosphate-buffered Saline(PBS) 0.01M has been chosen, and it is purchased from Sigma-Aldrich® company. By dissolving each tablet of PBS in 200ml of deionized water, we reach PBS 1X, which has a concentration of 0.01M Phosphate-buffered saline (abbreviated PBS) as a buffer solution (pH 7.4) commonly used in biological research.
PBS is a water-based salt solution that is found in powder and tablets containing disodium hydrogen phosphate, sodium chloride, and, in some formulations, potassium chloride and potassium dihydrogen phosphate. The buffer can maintain at a constant pH. The ion concentrations of the solutions match those of the human body. To have dopamine inside our solution, Dopamine hydrochloride has been dissolved inside the PBS, and its concentration has been increased by steps of 300 nM. Dopamine hydrochloride has been purchased from Sigma-Aldrich company.
In order to not have any interference with the ENGINI platform, The microelectrodes have been twisted to the wires of the potentiostat, and no other glues or paste has been used.
To measure the standard deviation of the electrochemical measurement at each concentration, the measurement has been repeated four times, and the averages of them has been

calculated. A high concentrated Dopamine(2μM) is prepared, and at each step 5μl of that is added to 10ml of PBS to increase the dopamine concentration by 300nM. To have a uniform solution of dopamine, after adding high concentrated dopamine solution to PBS, the solution is stirred by a magnetic stirrer for 15 seconds. After that, the FSCV measurements are repeated four times. A potentiostat measures the derived currents at each step, and in the end, the data related to the graph is stored in a file for post-processing by MATLAB.
The Matlab code for the post-processing is mentioned in Appendix A. By averaging the current at each concentration and plotting the current vs. dopamine concentration, we reach the calibration curve of our experimental setup.

2.4. Sensor Calibration

In evaluation of electrochemical sensors, specific features should be considered for the performance of the sensor. Selectivity, sensitivity and limit of detection are the most important parameters which should be considered:

- Selectivity: Sensor's ability to differentiate the desired analyte from other compounds.
- Sensitivity: Change in the sensor output current caused by a unit change in the analyte's concentration.
- Limit of Detection(LOD): The minimum analyte concentration that can be measured by the sensor.

To measure the selectivity of the sensor, a known concentration of the desired compound in the presence of other compounds should be measured.
To draw the calibration curve, the output current of the sensor in different concentrations of the compound is measured, and the graph of the output current with respect to the concentration shows the calibration curve of the sensor.
The sensitivity of the sensor is calculated using the calibration curve using the slope of the graph.
The limit of detection(LoD) of the sensor can be derived by dividing the standard deviation of the baseline measurements over the sensitivity of the sensor. The limit of detection is defined by the International Union of Pure and Applied Chemistry (IUPAC) as:

$$LOD = \frac{3 \times \sigma_{i_{blank}}}{Sensitivity} \tag{2.4}$$

3 | Electronic Design for Dopamine Measurement

A part of this thesis concentrates on optimizing the potentiostat designed for the ENGINI platform. The platform is a 3-tier network consisting of an external processor, cranial transporter, and mm-scale sub-dural implants for intracortical recording.
The thesis focuses on the sub-dural implants to measure the current and derive the faradaic current, which contains information about the dopamine concentration.

3.1. Cadence Virtuoso

In this thesis the circuit design has been done in Cadence® virtuoso. This design is based on the TSMC 180 nm BCD Gen II technology which is widely used for 20 years. Europractice® in partnership with Imec® provides the IC service for the Imperial College London where the ENGINI platform is based. The circuit design is composed of two steps which described below. In all the simulation the temperature is 36.9 degrees which is the temprature of the brain.

3.1.1. Schematic design

In the first step the schematic of the design is designed based on the ideal component. In the schematic design the parasitic components are neglected and some general libraries such as Analoglib and Basic libraries has been used for the simulation. $mimcap_2p0_sin$ component is used for the capacitors. This kind of capacitor is composed of metal-insulator-metal structure. MIM capacitors provide larger on-chip capacitance but requires more fabrication steps while the Metal-Oxide-Metal capacitors provide less capacitance while need less fabrication steps.
In this design $nmos2v$ and $pmos2v$ from the library of $tsmc18$ has been used for the transistors. The threshold voltage of these transistors are 600mV approximately and the

body of the transistor is connected to power supply or ground voltage based on the type of the transistor. This connection is mandatory to prevent any change in threshold voltage of the MOSFET and to avoid the current flow through the body diode. Since there is a common substrate for all the MOS devices of one kind, it is not possible to short the body and source of all the transistors.
After designing each block in schematic level, a series of simulations should be done to evaluate the specifications of the design. Virtuoso ADE Product Suite is used for doing different types of simulations. The first test is the DC analysis of the design. The operating point of the transistor are critical in power consumption and behavior of the transistor. In addition, DC analysis helps us calculate the dc offset of the amplifier and the bias voltages of the device. The next set of simulation is the transient analysis. This simulation shows the behavior of the circuit in the time domain. Since the designed potentiostat is a temporal based dopamine concentration calculator, this analysis was widely used in this design to mesure the accuracy of the design and measure the propagation delays. Another useful simulation type is the AC analysis. In this analysis the behavior of the circuit is evaluated in frequency domain. The designed potentiostat is working in 10 KHz frequency so the stability of the circuit and the the gain of the amplifier should be checked in this frequency. Last but not least, The noise analysis should be done on the circuit to compute the equivalent input noise and the output noise. to be able to extract the desired signal, signal to noise ratio is the most important factor in the design. We can analyse the contribution of each transistor on the total amount of the noise in the circuit and reduce the noise by improving the dimension of the transistors.
After designing the schematic of each block, a symbol of that block can be created to be used as a part of another more complex design.

3.1.2. Layout design

When the simulation results of the schematic are acceptable with respect the requirements the layout design of the schematic can be started. The library of the tsmc18 has its own standard layout for the transistor and it is possible to change just the width and the length of the transistors. As a result, the layout of the transistors and capacitors are extracted from the schematic.
To connect the components to each other, metal layer one and metal layer two has been used. two metal layers was need to not make any short circuit and make the layout design more simple. *Via*s has been used to connect the metal lines to each other and also to connect metal layer to poly silicon. To have a minimum area for the system the

components should be placed as close as possible to each other and the wiring become more complicated. This desire comes with the increasing effect of parasitic elements. To reduce this effect, it is suggested to use two different metal level in wiring two parallel wires. This will help to reduce the capacitive effect of the wires. Also, the components should be placed in a way that the minimum length of wire is used to reduce the resistance of the wires. It is possible to use guard rings and dummy transistor to reduce the noise and charge injection. *ConstraintManager* simplifies the design of the guard rings and creating the dummy transistors based on the requirements.
The design rules should be respected. Design Rules Checking (DRC) is an essential step in layout design. DRC verifies whether the drawn layout meets the constraints imposed by the process technology to be used for its manufacturing. Calibre® DRC has been used to check the design rules. this tool shows the errors such as minimum metal lines width and the distance between them and any other constraints related to the fabrication process.
After completing the layout design and solving issues related to the DRC, The layout should be matched with the transistors defined in the schematic. We used Calibre LVS which is taking the layout and schematic of the design as inputs and the output is any possible mismatch between them.
By passing the DRC and LVS checks, the layout is ready for the post-layout simulation. For doing the post-layout simulations we need to extract the parasitic components present in the layout. Calibre PEX creates a netlist from the layout that includes resistive, capacitive and coupled capacitive parasitic components. After extraction of the parasitic components, post-layout simulations can be done by affecting these components into the behavior of the device. For high performance designs it may be necessary to re-do parts of the layout to reduce the parasitics present.

3.2. IC design

This chapter proposes a dual slope Analog to Digital Converter (ADC) to measure the faradaic current. To reach the faradaic current, the capacitive current should be subtracted, and then the faradaic current can be measured using ADC. Since the capacitive current is significant with respect to the faradaic current in large scan rates, we can reach a better dynamic range of current by removing the capacitive current. A 5-bit controlled current source is designed to subtract the capacitive current.
The complete structure of the potentiostat is shown in Figure 3.1. In the first step, the current captured from the working electrode is processed, and the capacitive current is subtracted. The current source is step-wise, and the amount of its current can be con-

trolled using 5 bits. In the second step, the faradaic current is stored by the integrator, which has been designed using the folded-cascade operational trans-impedance amplifier and the capacitor. In the third and last step, the comparator determines the time it takes to discharge the capacitor, and based on the discharging time and the formula below, we can calculate the amount of faradaic current.

$$I_{INT} = I_{DIS} \times \frac{T_{DIS}}{T_{INT}} \tag{3.1}$$

In this formula, I_{INT} is the current that is captured from working electrode by the capacitor in 10μs. I_{DIS} is the constant discharging current that is responsible for discharging the capacitor in the second step and T_{DIS} is the discharging time. T_{INT} is the integration time of the first step that the faradaic current is being stored in the capacitor.

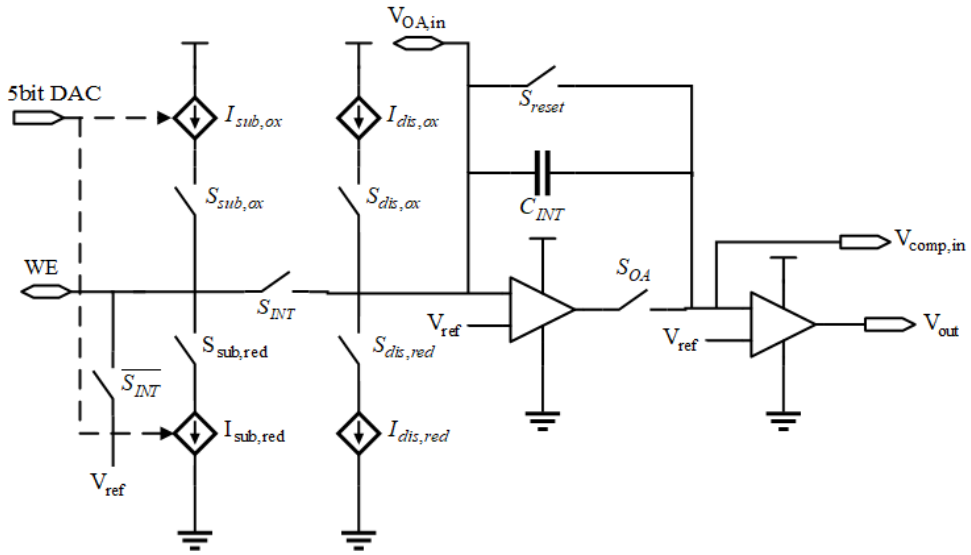

Figure 3.1: Dual-Slope ADC which is used to convert the working electrode current into a digital signal

S_{rst} is activated in the beginning to discharge the capacitor, and the voltage of the OTA in the input is equal to V_{ref}. After resetting the capacitor, the S_{rst} switch is turned off, and the integration of the faradaic current can be started. Depending on the oxidation or reduction voltage of the dopamine, the switches of the 5-bit controlled current source can be closed. The capacitive current is removed, and By closing S_{int} The current can be stored in the capacitor for a specific charging time, and the voltage of the input of the comparator goes higher than V_{ref}, and the out goes to a high state. By the end of the integration time ($T_{INT} = 10\mu$s), the integration switch is opened, and The discharging switches are turned on to remove the charge stored in the capacitor. The comparator is in

the high state during the discharging time until the capacitor is discharged entirely and the V_{int} can reach again to the V_{ref}. During the discharging time, the WE is connected to the V_{ref} to keep the cell in a balanced state. In our circuit, the discharging current is 10nA, the duration of the discharging time is equal to 80μs and C_{int} is equal to 1.5pF. Considering the current measured during the experimental analysis, The necessary capacitive current subtraction is around 2.56μA.

3.2.1. Current sources

In order to remove the capacitive current, we need a step-wise current source to remove this current. Also, we need discharging current sources to calculate the discharging time of the integrator capacitor. The proposed architecture in Figure 3.2 has been designed to create all these current sources. The biasing current of 80nA has been considered for the current source. By using the current mirror architecture with different multiplication factors, we can create different current suppliers. Switches D0-D4 can configure the necessary output current.
Depending on the oxidation or reduction we should have two different current directions for these two reactions. this is accomplished using the current mirrors to create a bidirectional current source.

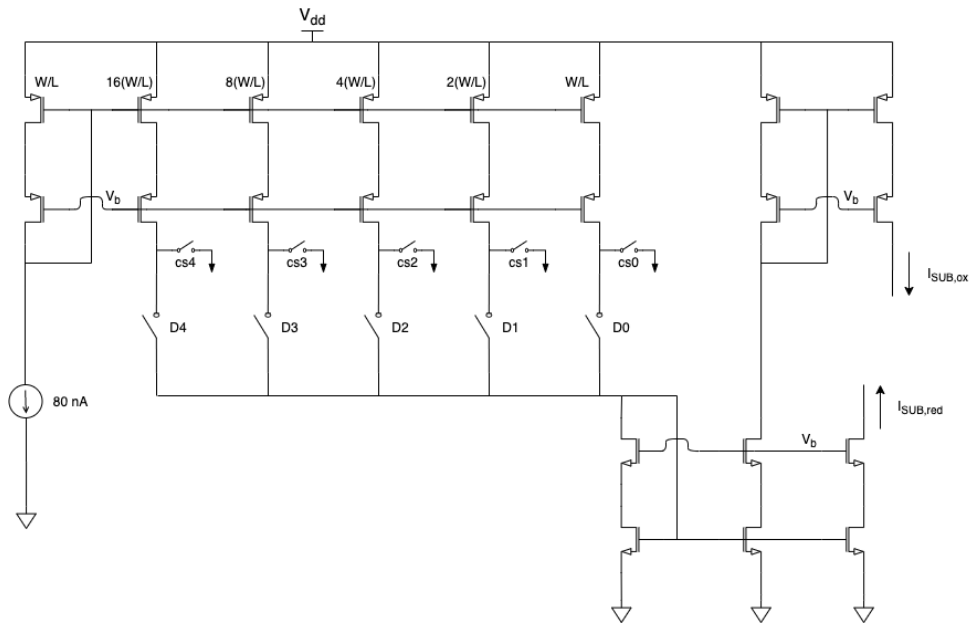

Figure 3.2: 5-bit controlled current source as a current subtraction unit. cs bits are used for current steering

When the switch is open, the charge is accumulated above the switch, which can create significant spikes by closing the switch, and this spike is destructive to the measurement. We use a partial-current-steering method to eliminate the accumulated charges above the switches with a careful timing arrangement. In this method, an auxiliary switch is considered beside each switch, and the same load of the main switch is connected to the auxiliary switch. Before closing the main switch, the auxiliary switch is closed to deplete the excess charge above the switch, and then the auxiliary switch can be opened, and the main switch is closed. It will be helpful if the two switches have a slight overlap to ensure no charge above the switch. Since the switch should be closed precisely before the main switch, it should have a proper timing arrangement.

After designing 5-bits controlled current source, it is connected to the the whole device using two switches. These switches is activated depending on the activation or reduction. The most important point about that is that PMOS transistors have been used for oxidation switch while NMOS transistors has been used for reduction switch. To reduce the amount of charge injection, two dummy transistors has been considered for each switch. The width of the dummy transistors should be half of the main transistor since half of the charge injection flows towards each direction. The structures of the switches are depicted in Fig. 3.3

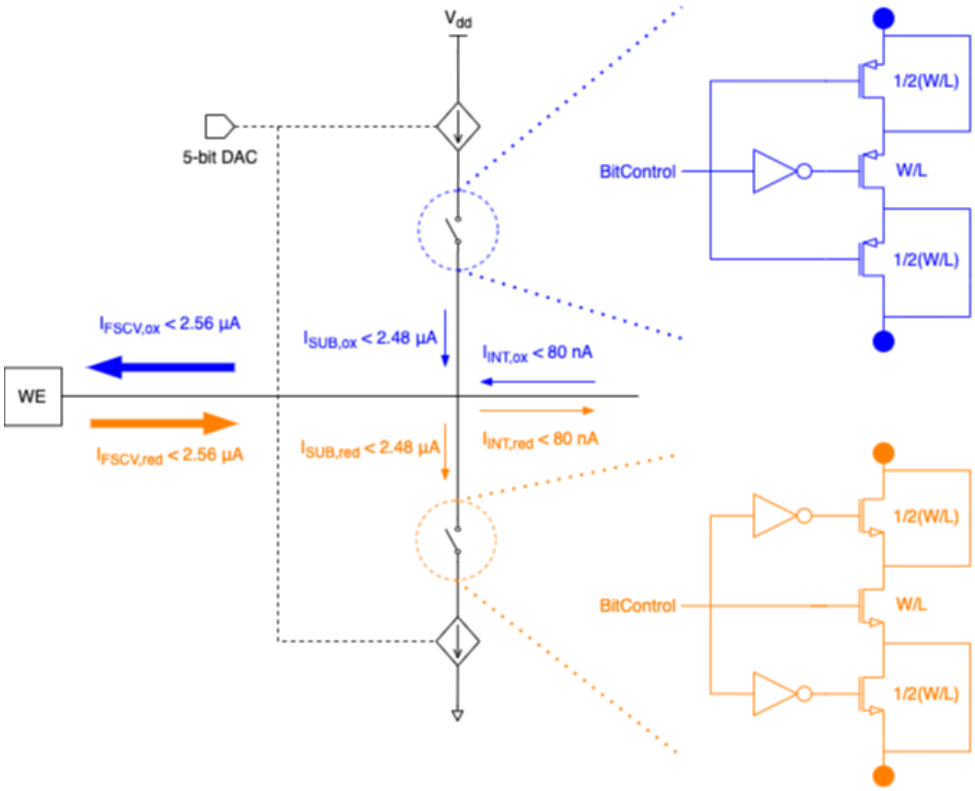

Figure 3.3: Switches used in the whole system

The layout of the NMOS based switch has been shown in Fig 3.4. Since the switches are controlled by microcontroller and the control pin of switch is changed by a very short rising and falling duration, the minimum dimensions has been considered for the inverter and the transistors of the switch. Also the body of PMOS transistor is connected to power supply and body pin of NMOS transistor is connected to the ground voltage to reduce the charge leakage through the body.

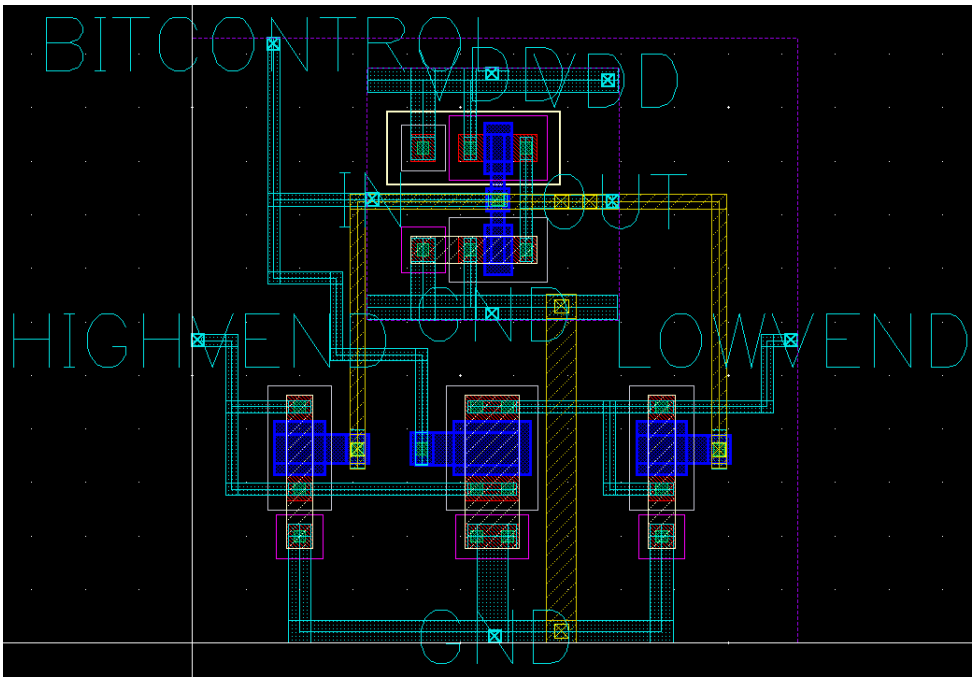

Figure 3.4: Layout view of the NMOS based switch

There is another set of current sources with a constant 10nA current supplying for discharging the capacitor. Since our implantable probe needs to work without any external current sources, we must create the discharging current source internally. Figure 3.5 shows the designed circuit for current biases in our device. V_b has been set using adjusting the dimensions of trans-diodes. A PMOS has been used for generating the desired bias current. By connecting the source pin of PMOS to V_{dd} and the gate pin of PMOS to created bias voltage the specific bias current is generated. In the next step, by multiplying the currents using the current mirrors, we reached 10nA and 80 nA current biases.

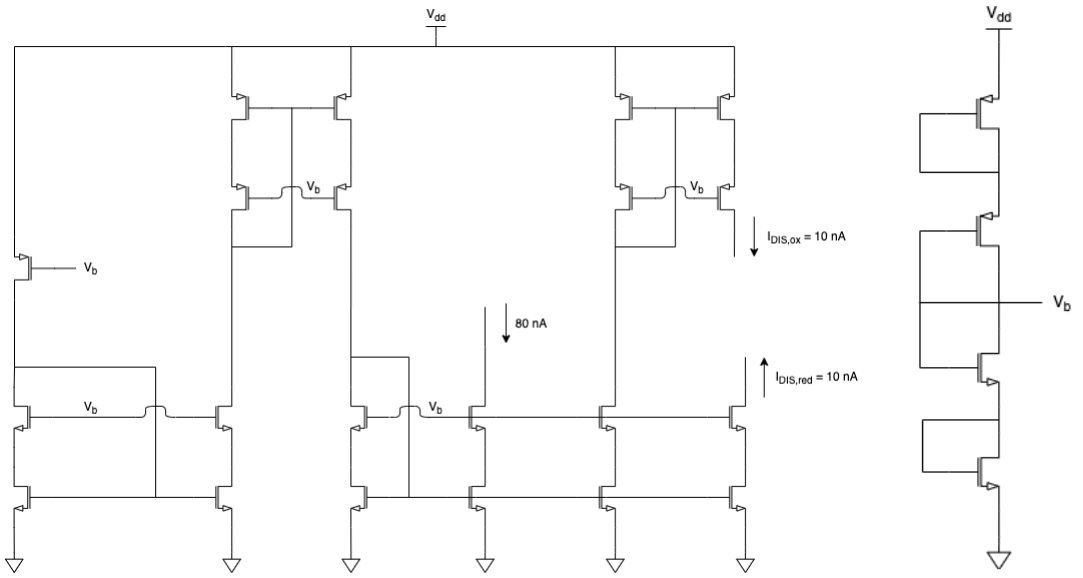

(a) Current biasing and discharging current source creation (b) V_b voltage

Figure 3.5: Biasing circuits for both current and voltage

In layout design, Some special techniques have been used to reduce the noise of the circuit and minimize the charge injection. Guard rings are used to prevent the injection of minority carriers from one type of transistor into the other type, where they become majority carriers and interfere with the correct operation of the transistor. In creating the guard ring based on the existing transistor inside it the type of Guard ring is chosen. If the guard ring is surrounding the NMOS transistors since the NMOS transistor has the p well the guard ring should be p type. If the guard ring is surrounding PMOS transistors, since the PMOS transistor has N well area the guard ring should also be N well type. Transistors with similar behavior, such as differential pairs and current mirrors, have been designed based on the common centroid configurations to prevent imperfections such as mismatch, offset, instability, and possibly latchup. Dummy transistors have been introduced for these groups of transistors to maximize the matching of short-distance etching gradients and stress effects. The layout of the entire current source is depicted in Fig.3.6 . As shown in this figure the main current mirrors to generate bit-wise currents are placed in the center of layout and the main switches and switches related to the steering technique are placed below the design. The circuits of bias voltage and bias current are placed on the left side of the layout.

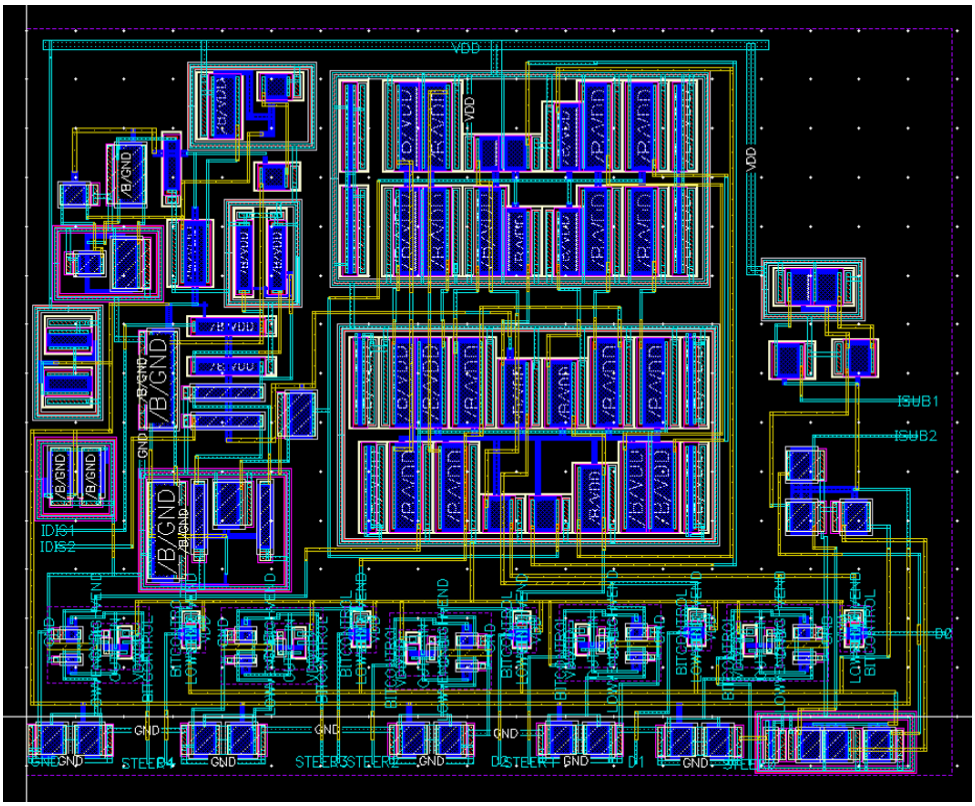

Figure 3.6: Layout design of current sources.

3.2.2. Folded-Cascode OTA

To convert temporal current information into the voltage, an integrator using Folded-Cascode OTA has been designed. The integrator consists of a folded-cascode OTA and a capacitor which is put in the feedback loop of the OTA.
The schematic of folded-cascode OTA is depicted in Figure 3.7. There are some considerations which has been taken into account in designing the folded-cascode OTA:

- All the transistors are in the subthreshold regime to minimize the power consumption of the implantable device.
- Noise in the circuit is reduced by choosing a PMOS transistor for the input of the OTA and choosing the channel length of the input transistor smaller than cascode mirror transistors.
- Since the output of the OTA is following the charging and discharging of the capacitors, the output voltage swing is optimized to keep the M11 at the edge of saturation.
- Differential gain is increased using the cascodes and large input transistors. Common

Mode Rejection Ratio is also improved by setting the bias current of M9 as small as possible. Unity gain (f_T) is also dependent on the input transistor. The circuit has several poles and zeros, but the output capacitance is the dominant pole.

$$\begin{cases} DCGain = gm_1 \cdot r_o, & \text{(3.2a)} \\ r_o = g_{m4} r_{ds4} (r_{ds11} \parallel r_{ds1}) \parallel (g_{m8} r_{ds8} r_{ds6}), & \text{(3.2b)} \\ f_T = \dfrac{g_{m1}}{2\pi C_L} & \text{(3.2c)} \end{cases}$$

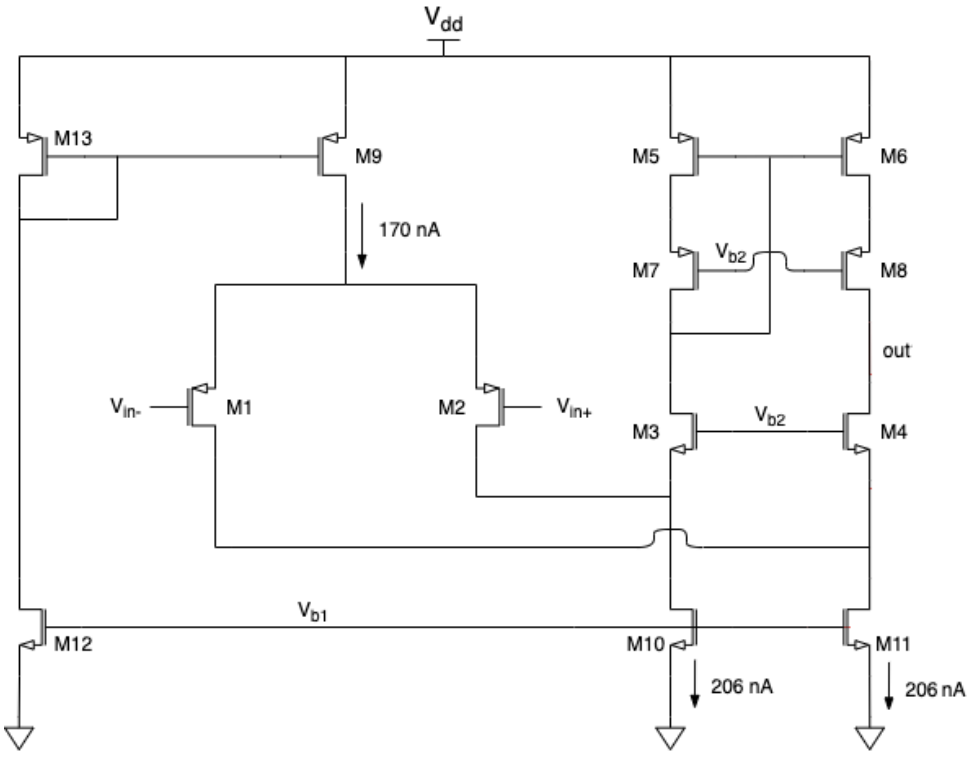

Figure 3.7: Schematics of the folded-cascode OTA.

The layout of the folded cascode OTA has been shown in Fig.3.8.

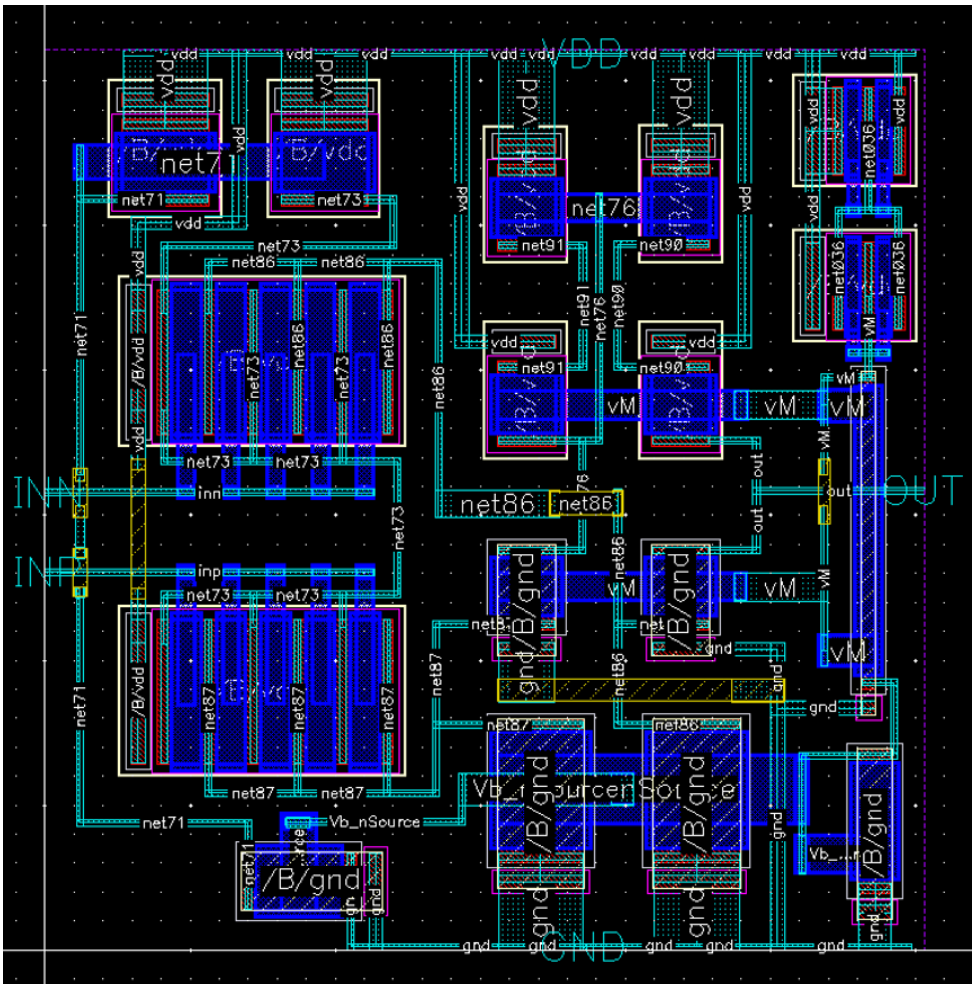

Figure 3.8: Layout of the folded-cascode OTA.

3.2.3. Comparator

The last component of the designed potentiostat is the comparator that can convert the analog potential into a digital format. One input of the comparator is connected to the reference voltage while the summation of capacitor voltage and reference voltage is given to the other input of the comparator. During integration time, the positive input of the comparator becomes larger than the negative input, and as a result, the output of the capacitor is set to high. In discharging phase of the electrochemical measurement, the capacitor starts to discharge, and the positive input voltage of the comparator starts to decrease until it becomes less than the reference voltage, and the output of the comparator sets to low. Since the concentration of Dopamine is measured based on the capacitor's discharging time, the comparator's delay time has a significant role in the electrochemical measurement. So in the designed comparator, the propagation delay is minimized. The schematic of the comparator is depicted in Figure 3.9. the comparator is composed of two

stages. In preamplifier stage the input transistor are chosen as PMOS to minimize the the equivalent input noise. V_b is created using the transdiodes and applied to the gate of current bias transistor of the first stage. Two current mirrors has been used in the first stage that amplifies an imbalance in the first stage and it improves the propagation delay of the comparator. Second stage is an amplifier stage which amplifies the differential output of the pre-amplifier and creates a rail to rail output for the comparator.
Since the propagation delay of the comparator has a significant importance in this application the current bias of the second stage has been regulated using the dimensions of the biasing transistor to decrease the propagation delay as much as possible beside respecting the standard allowable power consumption per area for implantable neural devices [5].

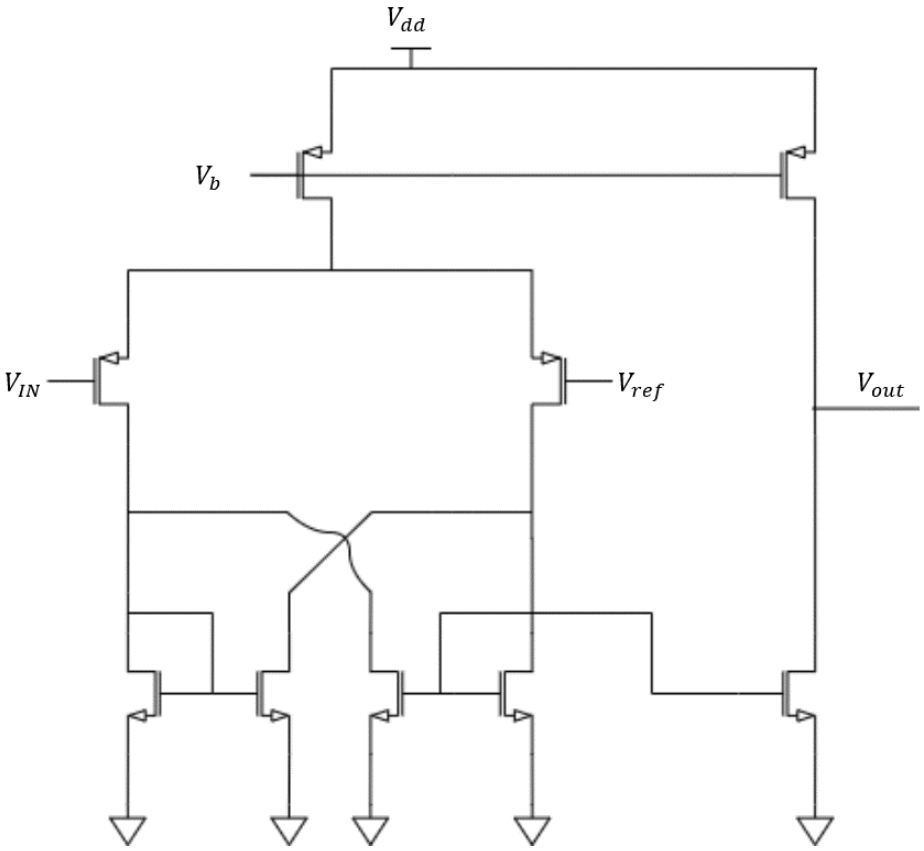

Figure 3.9: Schematics of the comparator.

In layout design of the comparator the finger transistors has been used to reduce the area. The body of the PMOS transistors are connected to highest voltage (V_{dd}) while the body of NMOS transistors are connected to the lowest possible voltage (V_{gnd}). The layout of the comparator has been shown in Fig 3.10.

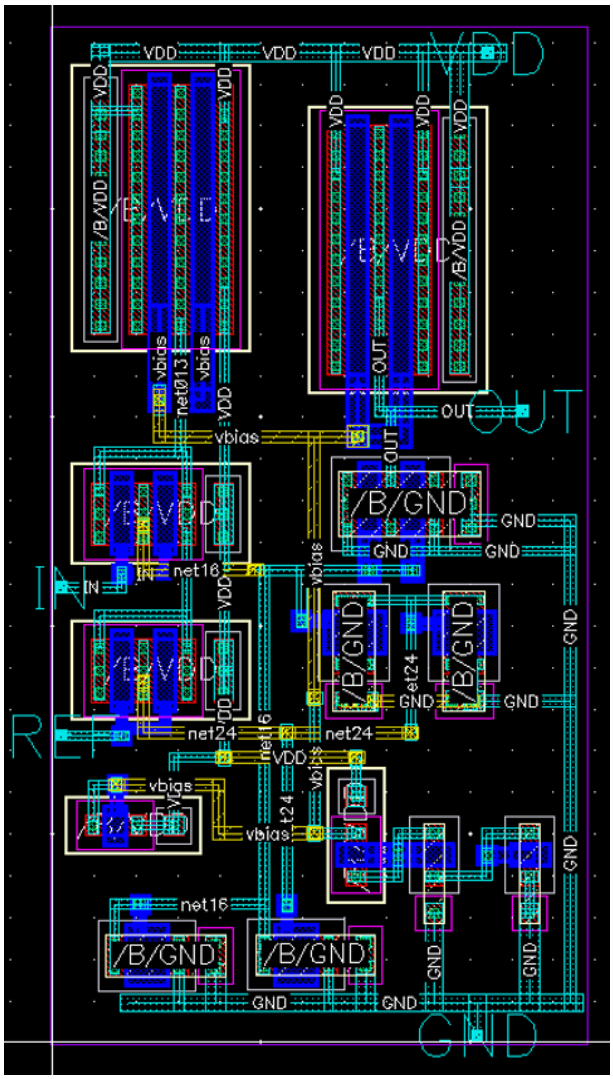

Figure 3.10: Layout of the comparator.

By assembling the different blocks of the layouts together we can reach to the proposed potentiostat which is shown if Fig 3.11. In this design the comparator and OTA are placed on the top to connect the pins of these two block to the capacitor with the shortest matal lines to the capacitor.

The capacitor has the metal-insulator-metal structure. Since the area of the metal plate is large, Antenna effect should be avoided in connecting the metal lines to the capacitor. The metal layers of the MIM capacitor should be always balanced to not have any antenna errors. To do this, the metal line of the bottom layer is brought to the top layer metal using the via and then both metal lines are brought first and second metal lines level to be connected to the whole system.

On the bottom of the designed core the current sources are placed. All the switches of the current source and the switches of the whole system are controlled digitally. The

digital parts are marked using SSUB2 layer. SSUB2 is not a physical layer but it helps the designers to detect the digital parts from the analog parts and it can be useful to eliminate the warning of the DRC check to separate the digital part from the analog part.

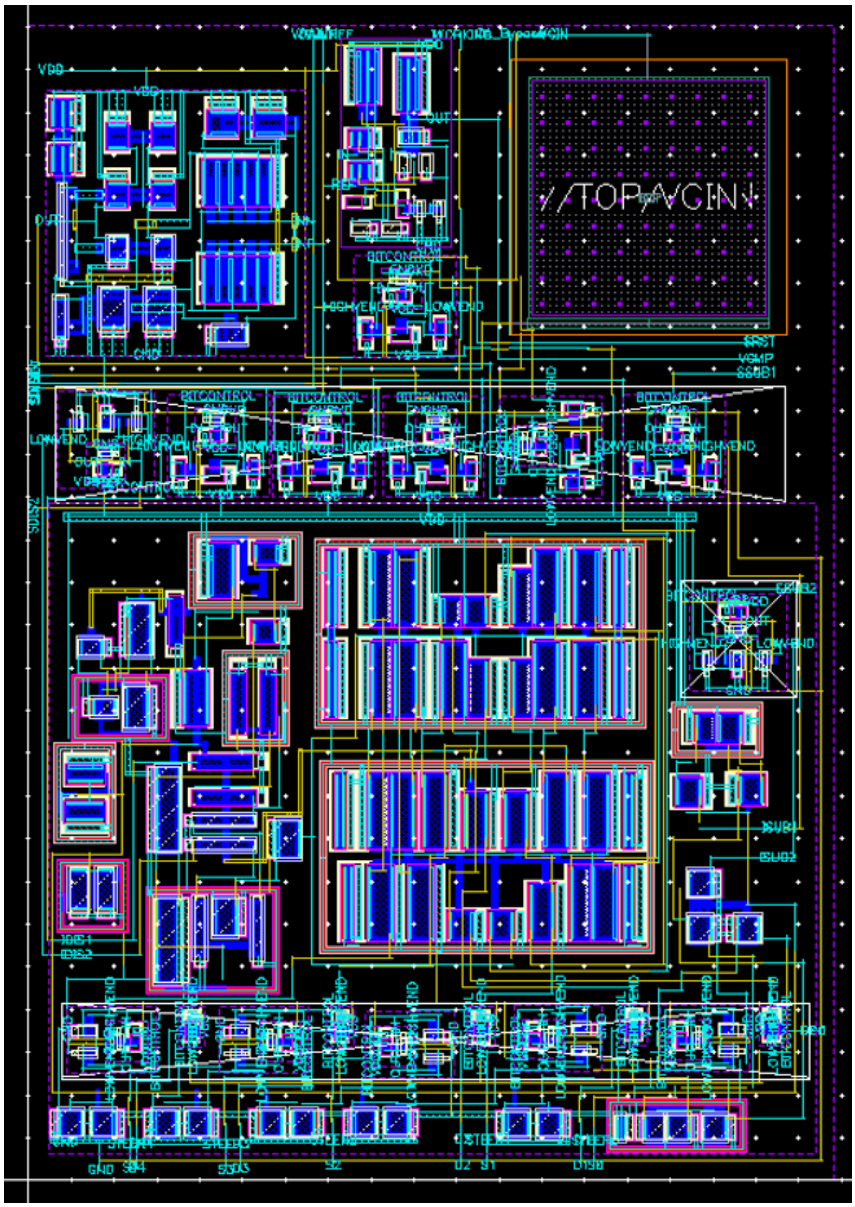

Figure 3.11: Designed layout of the potentiostat by using TSMC 180nm technology.

In the design of the pad ring, electrostatic discharges (ESD) protection system has been used for the analog pins. Electrostatic discharge originates from the fact that materials can carry static positive or negative charges resulting in a built-in voltage. The amount of this static charge depends on the material characteristics and external parameters like relative humidity. As soon as the charged material is in contact with a grounded object, the accumulated charge is depleted toward the ground. The discharge is extremely fast

and can damage the circuit.[35]
The I/O cells have been considered for both analog and digital pins. The digital I/O cell improves the pin's rising and falling time using the internal dedicated buffer. In order to be compatible with the circuit specifications of the ENGINI platform, a rectangular padring has been designed that contains the core system and bypass capacitors to create a stable power supply and filter the noise present in the power supply node. Since the power supply should be always constant and stable it is suggested to make the capacitance of bypass capacitor as large as possible to filter high frequency noises. To do this all the empty space in the padring has been filled with the bypass capacitor. The bypass capacitor is composed of 64 capacitors in parallel that create an 114.8pF equivalent capacitor. The designed layout of the whole circuit is shown in Fig 3.12.

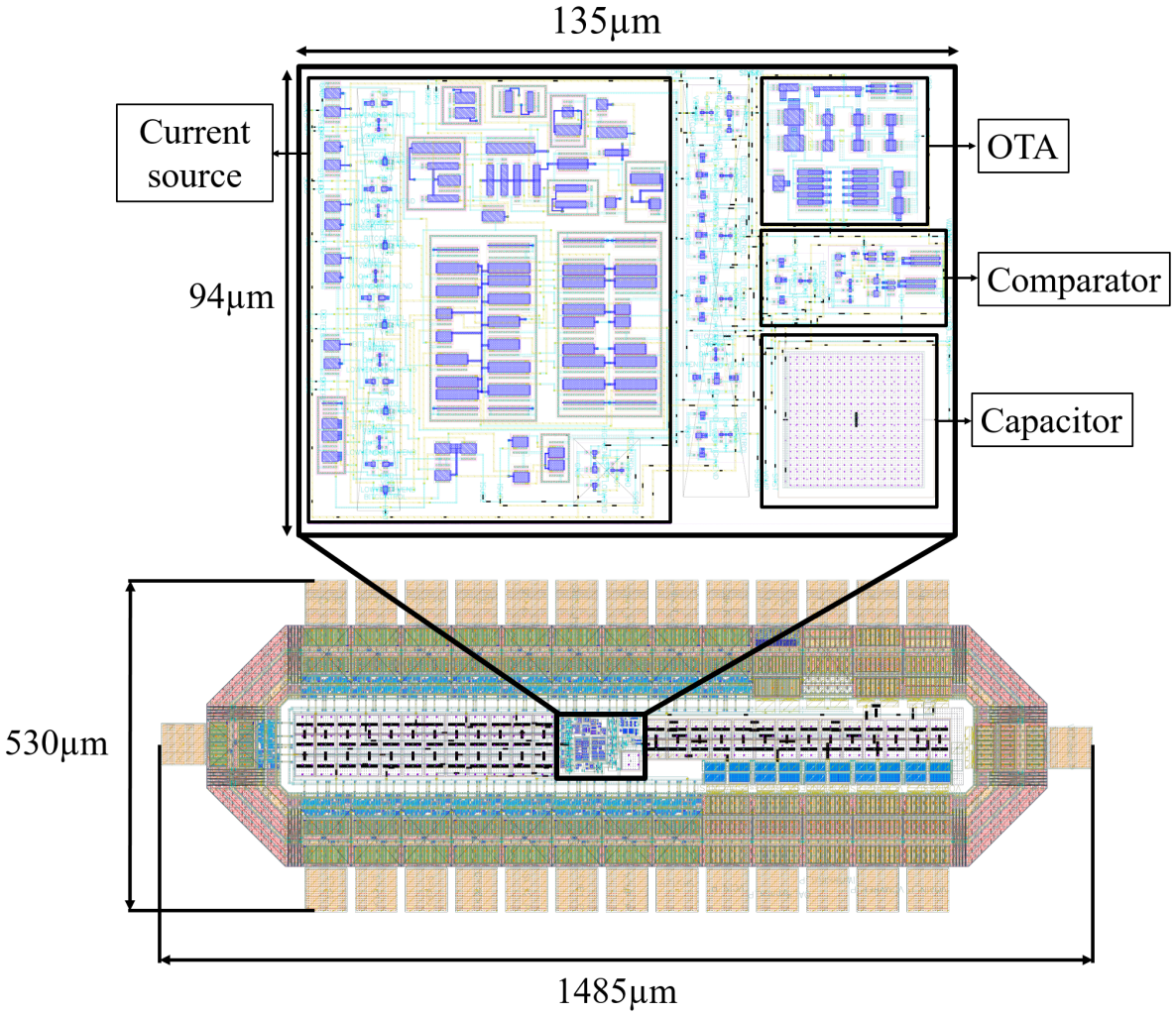

Figure 3.12: The whole designed layout. The system core and bypass capacitors are placed in the padring

This designed potentiostat is a part of the ENGINI platform. After measuring the dopamine concentration, the data is sent to the external part wirelessly. In the external part this data are processed using the deep learning algorithms and the amount of dopamine concentration is calculated based on the temporal output of the potentiostat. The whole design of the ENGINI platform has been shown in Fig 3.13. The eutectic seal prevents the moisture from reaching the active electronic part. The choice of low-temperature goldtin eutectic as the sealant ensures compatibility with CMOS,long-term reliability and resistance to corrosion.[38] The humidity seal measures the chip's humidity to control the probe's environmental situation. The wireless communication system can send the data and receive power from the external part. The coil is an electroplated Au film which inductively harvests near-field wireless power around the 433 Mhz ISM (industrial, scientific and medical) radio band. The optimal frequency for the ENGINI platform is 433MHz which is determined based on the maximum amount of power delivered to the load (PDL) within the specific absorption rate (SAR) limits, while also complying with the closest ISM band. A passive intermediate transceiver focuses the external power source and boosts the overall power transmission efficiency to provide a uniform power distribution.[15] The designed potentiostat is placed on the top of the ENGINI platform. The area of the whole ENGINI platform is 12.25 mm^2. The designed potentiostat occupies 0.75 mm^2 of the entire platform.

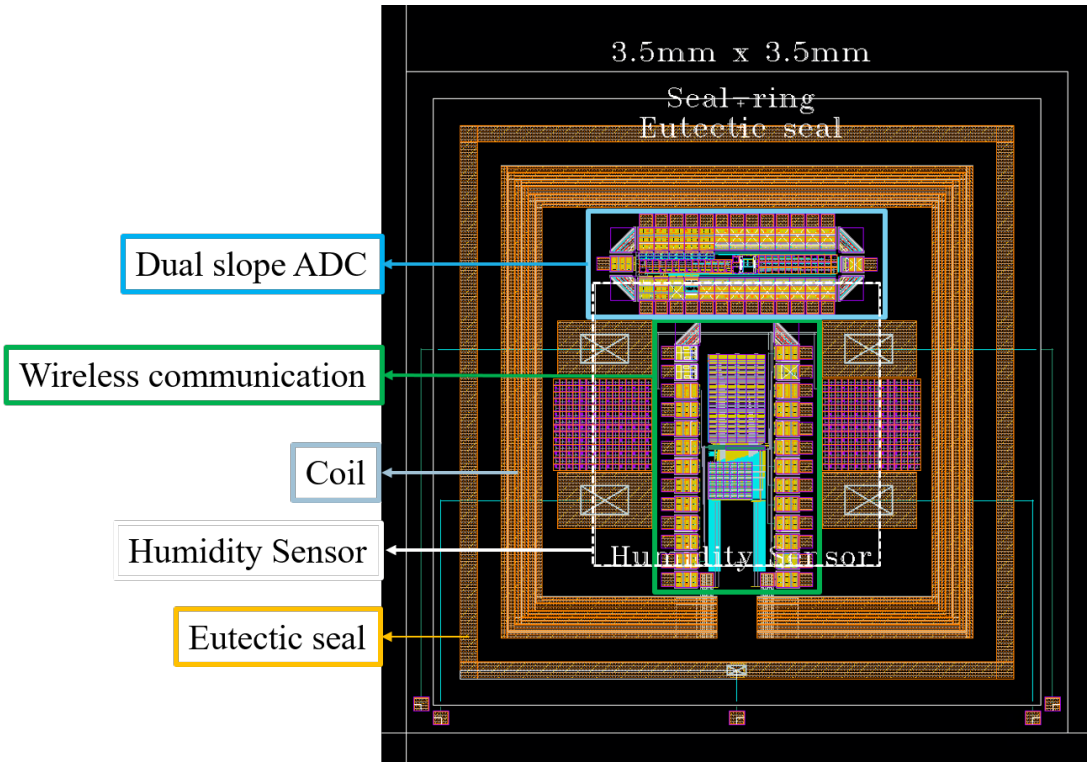

Figure 3.13: First designed ENGINI platform to measure dopamine and send it to external part wirelessly

3.3. Test Board Design

3.3.1. IC packaging

IC packaging is the last step of semiconductor packaging. The package surrounds the circuit material to protect it from corrosion or physical damage and allows mounting the chip to the printed circuit board (PCB). There are different IC packages, such as a pin grid array, quad flat pack, and ..., which have different pins. In this project, a JLCC68 package has been used, a lead-frame quad flat package containing 68 pins. A bonding diagram has been used to connect the pins of the IC to the pins of the package, and it makes the IC able to be mounted on the printed circuit board. The bonding diagram of the system is depicted in Fig 3.14.

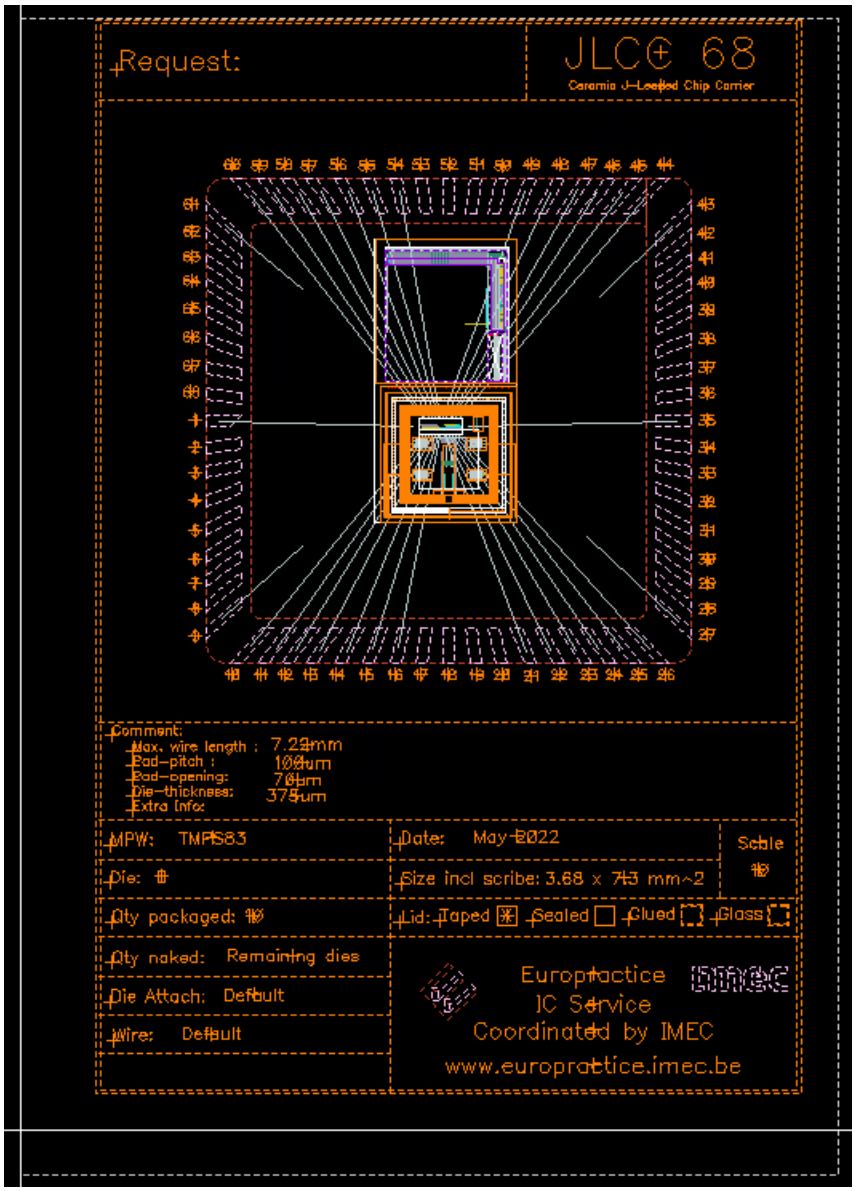

Figure 3.14: Bonding diagram of the designed circuit for JLCC68 package.

3.3.2. Board design

The CMOS-designed integrated system has been sent to Europractic® IC service for fabrication. To test the integrated chip in-vitro, a test board is needed to control the switches based on the timing specifications. Since the designed system is working based on the temporal measurements to calculate the dopamine concentration, minimizing the delay of the circuit has the highest priority. In addition, The test board should be able to supply power for the analog and digital parts of the device separately. In the IC design, some pins have been considered to check the functionality of each block separately, so analog pins on the test boards are needed to read the value of the pins' voltages and

currents separately.
To satisfy these requirements, Arduino® MEGA 2560 has been considered to control the switches and provide complete device monitoring. This micro-controller can isolate the analog and digital pins to reduce the amount of noise. Furthermore, the digital pins' rise time and fall time are approximately 40 nanoseconds, which is acceptable for our circuit since this delay causes a negligible error in dopamine concentration calculations. Since Arduino Mega micro-controller power supplies pins can provide only 5 volts and 3.3 volts, two analog pins have been considered to supply the 1.8 volts for the ESD protection block and the core block. To install the integrated chip, an Arduino shield board has been designed using Altium® Designer software to be attached to the Arduino board easily and minimize wiring noise. Analog pins of the system have been used for the following purposes:

- Working electrode pin to collect the current produced by the redox reaction.
- A pin to set the reference voltage of the designed circuit.
- $V_{OA,in}$ pin to read the faradaic current in case of failure in the functionality of the OTA.
- $V_{comp,in}$ pin to read the voltage dropped on the capacitor to calculate the amount of charge stored in the capacitor.
- An analog pin to act as a power supply for the system core to be set on 1.8 volts.
- A pin to be set on 1.8 volts and work as the power supply for the ESD protection blocks.

A series of digital pins has been used for the following functionalities:

- 5 digital pins for controlling the switches responsible for setting the amount of current of the 5-bits controlled current source.
- 5 digital pins for controlling the switches of the current steering part of the current source to reduce the spiking currents produced in the output of the current source. These switches can be active for a short time before activation of the main switches of the current source to discharge the charge accumulated on the drain of the transistors.
- 8 pins to control the switches in the integrated chip to effectively activate each step of measurement time.

- A pin set in digital input pin mode to be connected to the output chip to read the duration of the time that the output is in high level which is proportional to the current produced by the redox reaction and so the dopamine concentration.

The designed printed circuit board has been shown in Fig. 3.15.

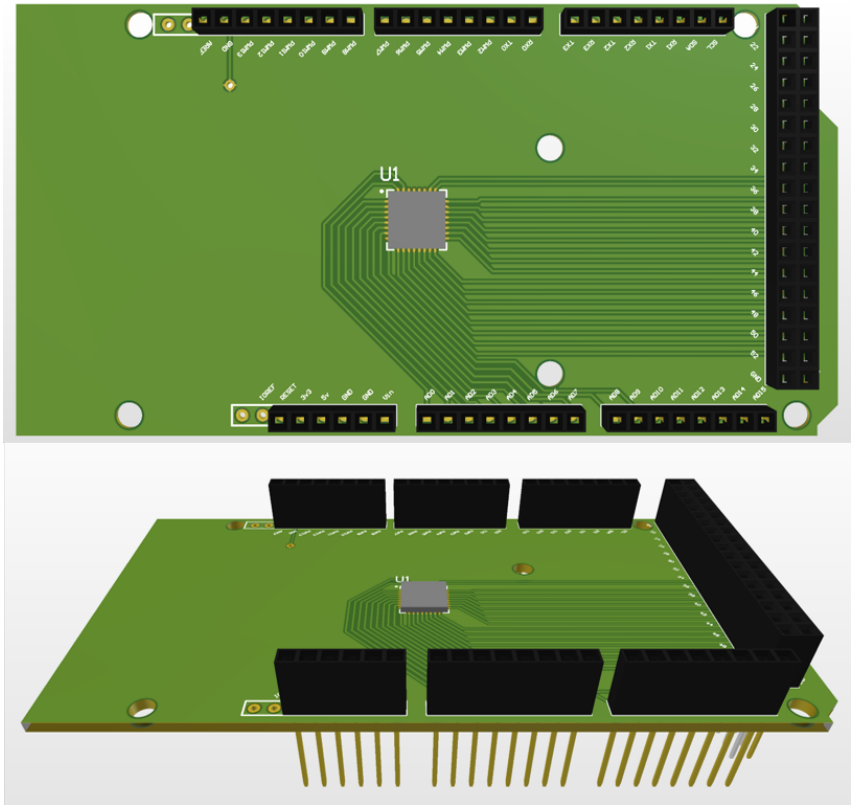

Figure 3.15: Arduino shield board designed as a test board for the integrated circuit.

4 | Results

In this chapter, the results of the circuit design and electrochemical measurements have been discussed. The results derived from the electronic circuit simulation are divided into pre-layout and post-layout simulations. The electrochemical measurement results have been reported in the following, and the compatibility of these results with the electronic simulation results is confirmed.

4.1. Circuit simulation results

The simulation of the designed circuit was done at the schematic and layout levels. At the schematic level, the circuit's functionality is tested regardless of the parasitic components. The performance of the potentiostat was also investigated with post-layout simulations. The layout was optimized to have the best performance based on the needs of the ENGINI platform. The post-layout simulation Calibre Parasitic Extraction (Calibre PEX) tool was used to extract the parasitic components. The performance of individual components and the entire circuit is presented in this section. The post-layout simulations include Resistive (R), Capacitive (C), and Coupled Capacitive (CC) parasitic elements.

4.1.1. 5 bits controlled current source

In order to remove the capacitive current of the current received from the microelectrodes, an adjustable current source is needed. A 5-bit DAC with the least significant bit corresponding to 80 nA is used for this purpose.
The most important point of care is to eliminate the spikes which originate from the charge accumulation on the drain pin of the switches before activation. To reach this goal, the partial current steering method has been used. Since The redox current has both negative and positive currents, the current source should be able to provide the current range in both directions, which has been possible using the current mirrors. When the charge is stored in the capacitor, a constant current source is needed to discharge the capacitor. In order to be compatible with the reduction and oxidation current, the discharging current has been considered in both directions. The pre-layout simulation results of the current

source have been shown in the Fig 4.1.

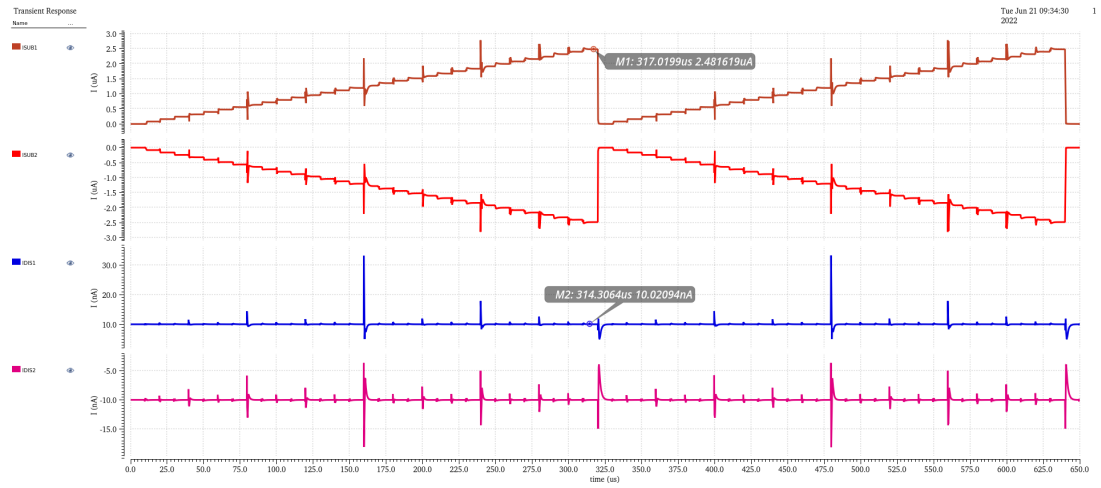

Figure 4.1: Pre-layout simulation results of the 5 bit controlled current source.

Pre-layout simulations show that the current source can provide current from 80nA up to the 2.48 μA, and the discharging current is in the order of 10nA. The Pre-layout simulation shows that The spikes related to the charge accumulation on the switches have been reduced significantly and the remained spikes are negligible.
In the post-layout simulation, The resistive, capacitive, and coupled capacitive parasitic components have been considered. The maximum current that can be supplied in post-layout simulations is 2.34 μA, and the discharging current is 8.87 nA. The post-layout simulations show that the designed current source satisfies the current requirements of the electrochemical dopamine measurements. The results related to the post-layout simulations have been shown in Fig.4.2 .

Figure 4.2: Post-layout simulation results of the 5 bit controlled current source.

Monte Carlo analysis is based on statistical distributions from the fabrication processes distribution. It realistically simulates mismatching and process variation. Each simulation run calculates every parameter randomly according to a statistical distribution model. To have a realistic distribution of the result, 200 samples are required. This means that the simulation will be repeated 200 times, and at each simulation, a characteristic of the design related to the mismatches or fabrication process will be changed.
A Monte Carlo simulation has been done for the current source's bias voltage to guarantee the bias voltage's accuracy. The result of this simulation is shown in Fig 4.3. Based on Monte Carlo simulation results the mean value of the bias voltage is 904.26 mV and the standard deviation is 18.2 mV which shows 2% deviation from the nominal value.

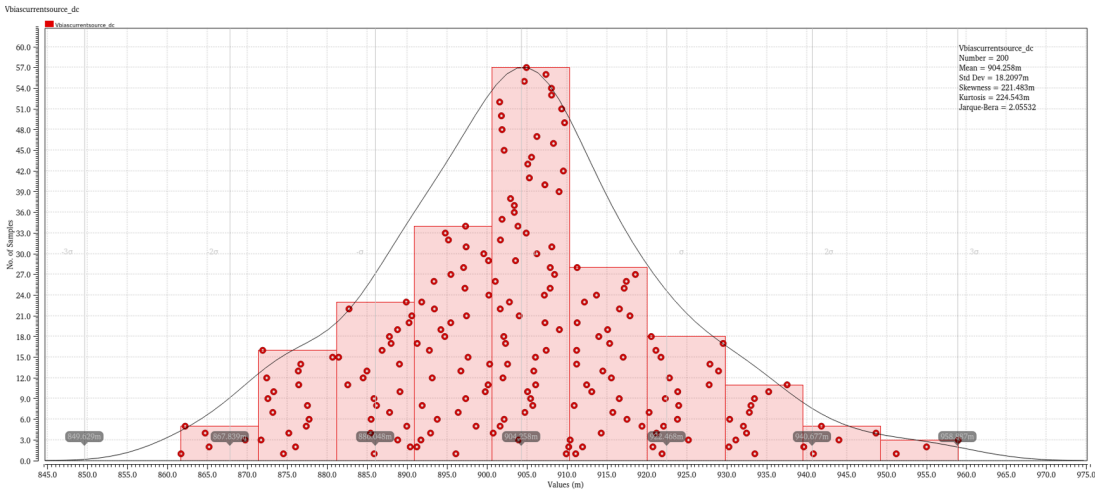

Figure 4.3: Monte Carlo simulation for the bias vltage of the current source

4.1.2. Folded cascode OTA

The folded cascode operational transimpedance amplifier has been designed to convert the temporal current information to the voltage by utilizing a capacitor.
Post layout simulation of the bode plot for OTA which is showed in Fig. 4.4 results that this block has a DC gain of 51dB and the phase margin of OTA is 141° at the working frequency of potentiostat (10KHz). This data shows that the OTA preserves a high gain at our working frequency in addition to a large phase margin in this frequency. As a result, the poles do not affect the gain in this frequency.
A full details of pre-layout and post-layout simulation results of OTA has been described in table 4.1

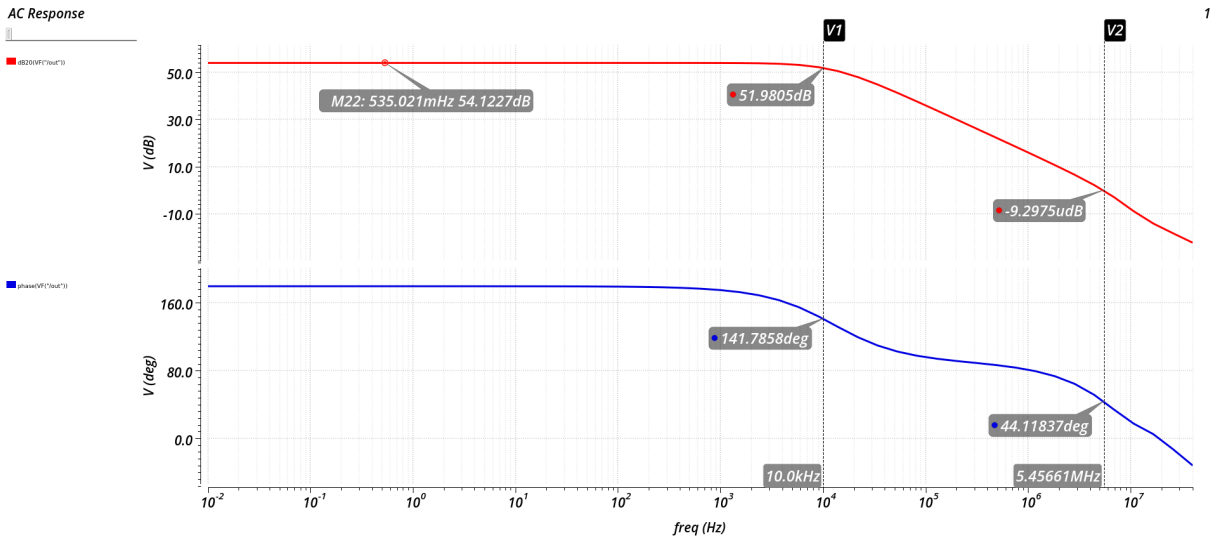

Figure 4.4: Post-layout simulation of bode plot for Folded cascode OTA

Specifications	Pre-layout	Post-layout
DC Gain	90 dB	54.1 dB
CMRR	147.6 dB	102 dB
Phase margin	45.6°	46.7°
Gain margin	16 dB	14.28 dB
GBWP	5.15 MHz	4.36 MHz
Slew rate	8.74 V/µs	7.22 V/μs
Power consumption	1.19 µW	1.10 μW
Area	-	942 µm^2

Table 4.1: Pre-layout vs post-layout simulation results of the folded cascode OTA

4.1.3. Comparator

The last block of the designed potentiostat is the comparator. By using the comparator, we can measure the duration of the discharging of the capacitor, and based on the equation 3.1 the current related to the redox reaction can be calculated. This current is proportional to the dopamine concentration.

Since the dopamine measurement is based on the temporal measurement, the delay of the comparator is the most important specification of the design of the comparator. In this regard, The design of the comparator focused on the rise time and fall time of this block.

The pre-layout and post-layout simulation results are reported in table 4.2

Specifications	Pre-layout	Post-layout
Input offset voltage	11.2 μV	861 μV
Equivalent input noise	45.3 μV	50.6 μV
Input capacitance	13.8 fF	14.6 fF
Propagation delay	378 ns	388 ns
Power consumption	4.78 μW	5.07 μW
Area	-	313.7 μm^2

Table 4.2: Pre-layout vs post-layout simulation results of the comparator

To monitor the effect of the fabrication process on the bias voltage of the comparator, a Monte Carlo simulation has been done on the bias voltage. It shows that the fabrication process and deviation of the characteristics of transistors have a negligible effect on the value of the bias voltage. The Monte Carlo simulation results have been shown in Fig 4.5. The standard deviation is 11 mV, and the mean value is 1.377V.

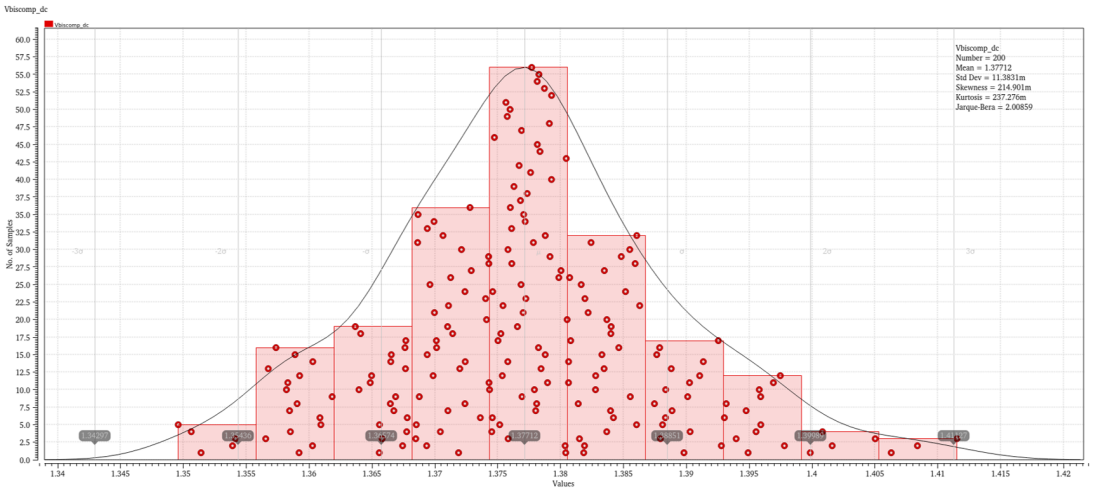

Figure 4.5: Monte carlo simulation of the comparator bias voltage by using 200 model samples.

4.1.4. System level results

In the system-level simulation, the potentiostat has been simulated by applying a constant current in the input of the system, testing the functionality of the current source,

calculating all the specifications of the whole system, and ensuring the correct working of the device. To this aim, post-layout simulations have been done on the device. An input current source equal to 2.4 μA has been used in the system's input. The current subtraction can reduce the input current by 2.34 μA. The simulation result of this measurement is shown in Fig 4.6.

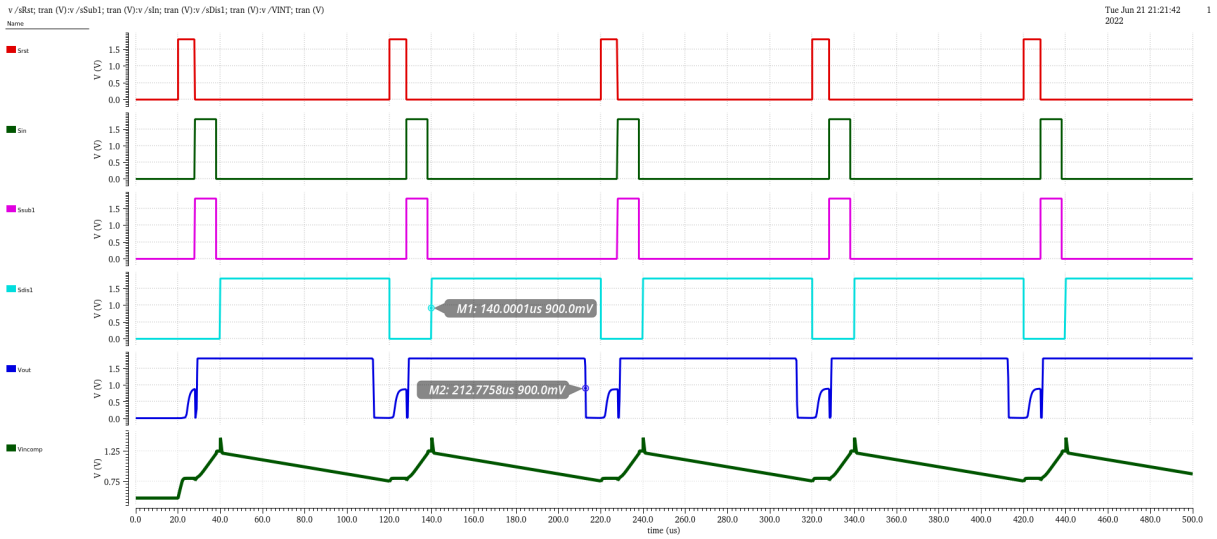

Figure 4.6: Post-layout simulation results of the whole system. Input current is 2.4 μA which is the maximum measurable current.

First, the reset switch (S_{RST}) is activated to discharge the capacitor. The system is ready to capture the redox current by opening the reset switch. S_{IN} is closed to record the current. Depending on the oxidation or reduction current S_{SUB1} or S_{SUB2} is closed to eliminate the background current. The maximum subtraction current in post-layout simulations is 2.34 μA. The background current is eliminated from the captured current, and the faradaic current passes through the capacitor. The voltage node of the input of the comparator goes up, and the system's output goes to a high level. The integration time is 10 μs. In the next phase, the integration switch is opened, and the charge stored in the capacitor starts to be depleted. To do this, S_{DIS1} or S_{DIS2} is closed depending on the oxidation or reduction current. The discharge of the capacitor continues for 80 μs, and by reaching the input voltage of the comparator to the reference voltage, the output of the circuit goes low. By calculating the time of high level and using the equation 3.1 the concentration of the dopamine can be derived.
The performance of the individual components and the whole device has been reported in table 4.3.

5-bit Controlled Current Source

Parameter	Pre-layout	Post-layout
Current range	80 nA – 2.48 μA	70 nA – 2.34 μA
Discharging current	10.01 nA	8.86 nA
Static Power Cons. Range	3.83 – 12.7 µW	3.65 – 16.26 µW
Area	-	7206 µm^2

Folded-Cascode OTA

Parameter	Pre-layout	Post-layout
DC Gain	90 dB	54.1 dB
CMRR	147.6 dB	102 dB
Phase margin	45.6°	46.7°
Gain margin	16 dB	14.28 dB
GBWP	5.15 MHz	4.36 MHz
Slew rate	8.74 V/µs	7.22 V/μs
Power consumption	1.19 µW	1.10 μW
Area	-	942 µm^2

Comparator

Parameter	Pre-layout	Post-layout
Input offset voltage	149 µV	861 µV
Equivalent input noise	2.85 mV	50.6 µV
Input capacitance	1.48 fF	14.6 fF
Propagation delay	352 ns	388 ns
Power consumption	1.92 µW	5.07 µW
Area	-	313.7 µm^2

The entire circuit of the potentiostat

Parameter	Pre-layout	Post-layout
RMS input noise	65 μA	89.8 μA
Power consumption[a]	1.01 µW	1.02 μW
Area of the core	-	12712 µm^2
Total Die Area[b]	-	0.75 mm^2

[a]Highest average power consumption. A duty cycle of 10% is assumed.
[b]Total pad ring and the core area

Table 4.3: CIRCUIT PERFORMANCE (POST-LAYOUT(R+C+CC))

4.2. Electrochemical results

This chapter will discuss the electrochemical results derived from in-vitro dopamine concentration measurement. To measure the dopamine concentration, Fast Scan Cyclic Voltammetry (FSCV) has been used to measure the faradaic current generated by the redox reaction of the dopamine. The scan rate of 50 V/s is considered since high surface reactivity causes the background current to reach the current limit of the FSCV apparatus. The staircase sweeping of the voltage is between -0.4V and 1.3V, and the graphs of the current with respect to the voltage can be sketched to find the current peak of the oxidation and reduction reaction.
The micro-electrodes that have been used for this experiment are as follows:

- Working electrode: Tungsten, 25μm diameter, 3.5mm length
- Reference electrode: Platinum, 25μm diameter, 1cm length
- Counter electrode: Platinum, 25μm diameter, 1cm length

The experimental setup is shown in Fig 4.7. A magnetic stirrer has been used for stirring the solution after each measurment to have a uniform solution during all the measurments. To keep the temperature similar to the temperature of the brain, The heater of the magnetic stirrer has been used to heat up the sultion up to 37 degrees. The microelectrodes have been twisted to a multicore wire to connect them to the potentiostat,

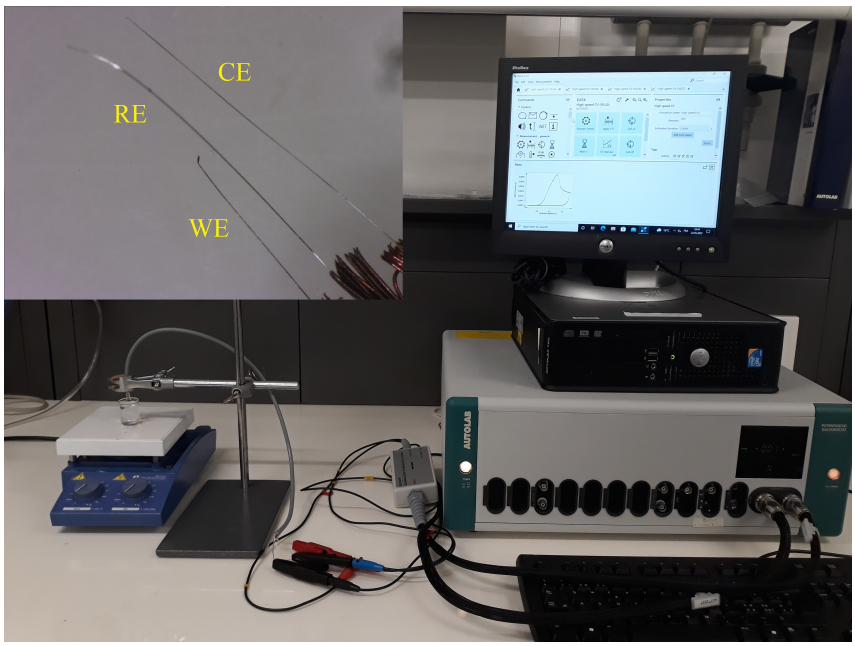

Figure 4.7: Experimental Setup for in-vitro measurement of dopamine concentration using the proposed micro-electrodes.

The positioning of the microelectrodes in the solution is depicted in Fig. 4.8. Since the electrodes are bare microwires, the area that is positioned inside the solution has a significant effect on the measured current.

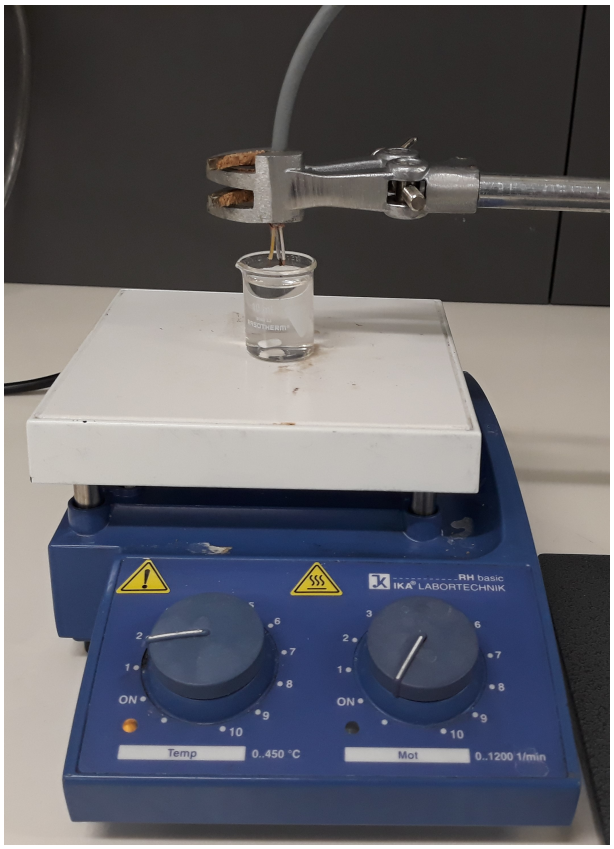

Figure 4.8: The experimental setup for evaluation the feasibility of dopamine concentration measurement by positioning the microelectrodes inside the solution and using magnetic stirrer to have a uniform solution during analysis. This setup can be improved by designing a system to hold the microelectrodes in an accurate position.

The background current has been stabilized by repeating the experiment for ten times. The picture of the background current has been shown in Fig 4.9. This graph shows that the tungsten can be only oxidized and there is not any reduction peak for the tungsten wire[19].

The anodic reaction of tungsten is as follows in reaction 4.1.[19]

$$W + 4H_2O \rightarrow WO^{2-}_{4(aq)} + 8H^+ + 6e^- \tag{4.1}$$

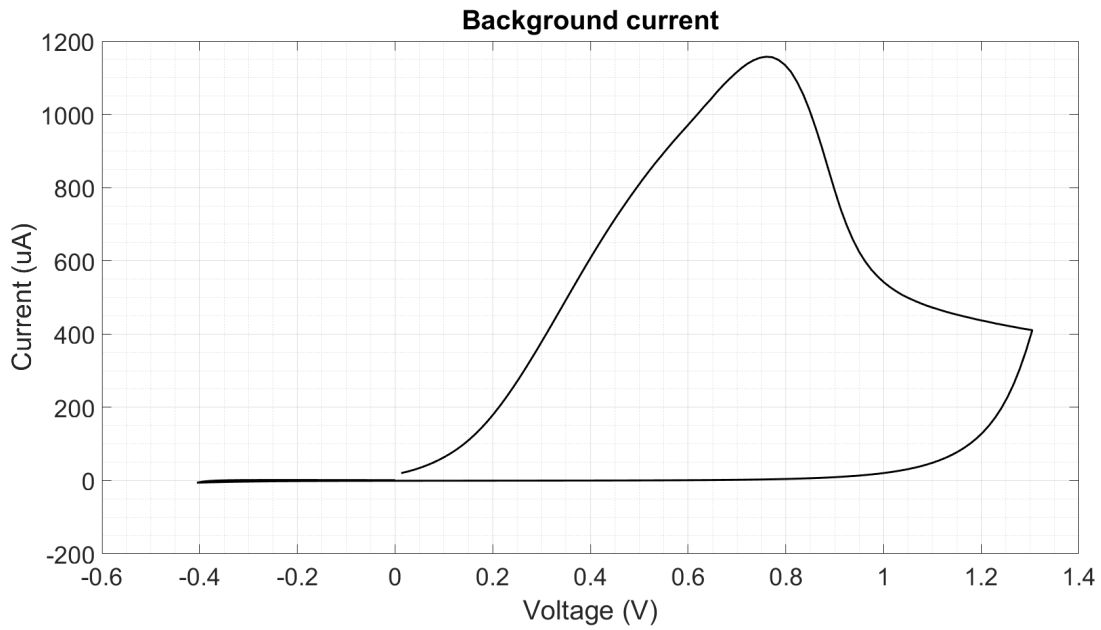

Figure 4.9: Background current produced by the redox reaction of the working electrode in 0.01M Phosphate buffered saline after stabilization of the microelectrodes.

After stabilization of the background current, the cyclic voltammetry was repeated four times for every concentration and the concentration of the dopamine is increased by 0.3 μM steps. In this experiment the temperature was kept at 37 degrees which is the temperature of the brain. The dopamine solution was light sensitive so it was kept in a dark area. The background-subtracted current for the concentration of 0.3 μM dopamine solution has been shown in Fig 4.10.

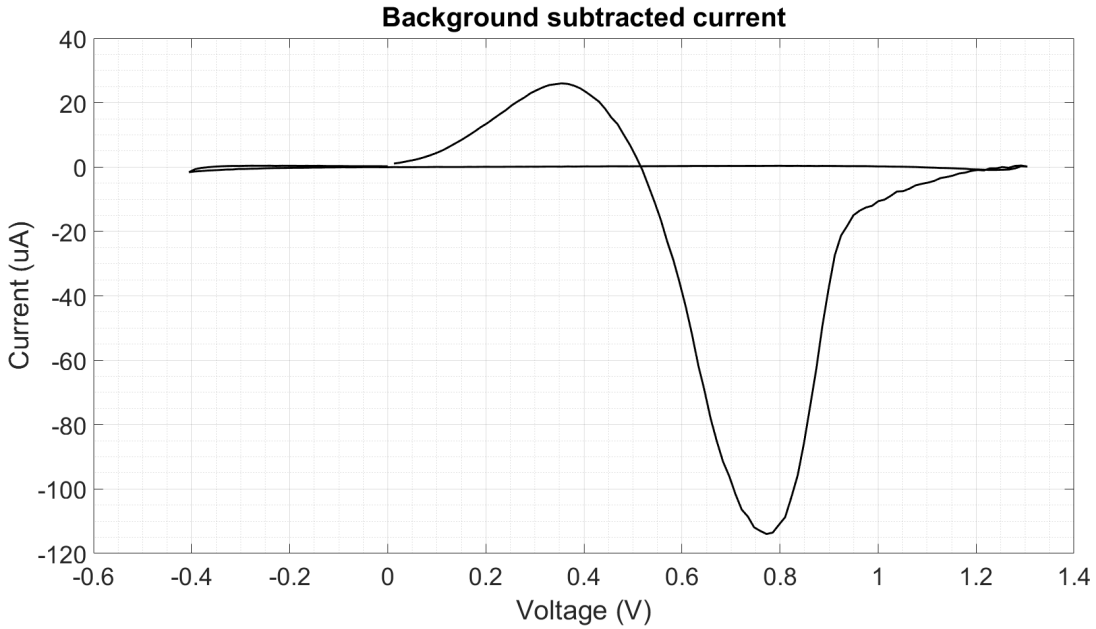

Figure 4.10: Background subtracted current for 0.3μM dopamine solution in PBS buffer pH 7.4 at 50 V/s. The current peak for the oxidation of dopamine is 26μA.

By increasing the dopamine concentration, The faradaic current increases proportionally. The Calibration curve is depicted by calculating the faradaic current's peak current and plotting the peak currents with respect to the dopamine concentration. The Calibration curve will be useful for calculating the sensitivity of the sensor and the Limit of Detection(LOD). The calibration curve of the designed experimental setup has been depicted in Fig. 4.11 . The fitting in the lower range has been done with 99.2% accuracy which is an acceptable fitting in data analysis.

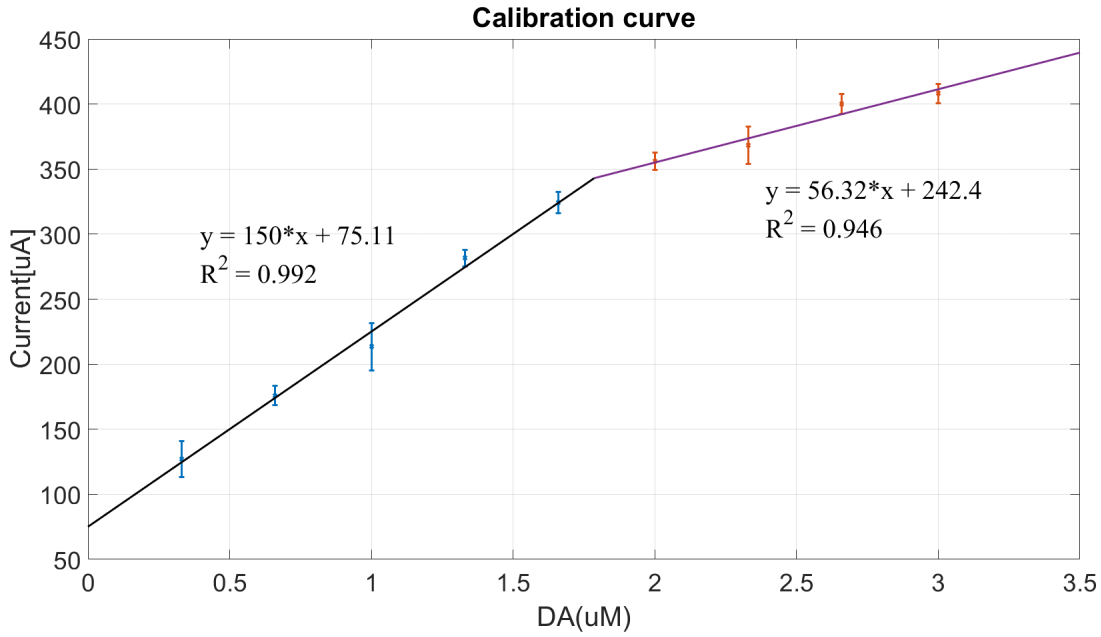

Figure 4.11: Calibration curve of dopamine at an oxidation peak voltage of dopamine. The experiment was performed in PBS buffer pH 7.4 at 50 V/s.

The calibration curve consists of two linear calibration regions. Since the Dopamine concentration in the human brain is up to 3 μM, The first linear part can satisfy our requirements.

The calibration curve's slope shows the sensor's sensitivity, which is 150 $\mu A/\mu M$ in a concentration window of μM-range, matching well with concentration ranges expected in the human brain.

The limit of detection can be derived from the equation 2.4. The LOD is estimated down to 33 nM, which fits very well also with concentrations in rats, where dopamine ranges from 50 to 100 nM.

By comparing the results derived from the experimental in-vitro analysis of microelectrodes and the electronic design simulation results of the potentiostat which has been designed for the ENGINI platform and are reported in section 4.1.4, we conclude that the designed electronic device satisfies the requirements of the dopamine measurements. The current peak of the total current that is passing through the electrode is 1.16 mA, which is proportional to the working electrode area in use ($0.275mm^2$). The background current was stabilized by repeating the cycling voltammetry ten times and after each measurement the solution is stirred using the magnetic stirrer to perform the analusis in the uniform solution. Since dopamine should be measured in the synaptic regions, the working electrode must have a few microns in length. By choosing the working electrode with an approximate area of 500 μm^2 as suggested in reference [42], the background current

will be 2.1 μA which can be subtracted from the signal using a 5-bits controlled current source.

5 | Conclusions and future developments

In this project, a new 3-electrodes sensor has been designed and tested for measuring dopamine in the physiological range in the human brain. An integrated CMOS potentiostat has been designed as well in order to measure dopamine concentration in future in-vivo experiments. The plan is to integrate this potentiostat into the ENGINI platform to monitor the dopamine concentration in vivo wirelessly. Post-Layout simulations show that the potentiostat eliminates the background current and measures the faradaic current produced by the dopamine redox reaction. In addition, electrochemical measurements have been done to measure dopamine concentration in PBS buffer. In-vitro experiments shows that the derived current range from the microelectrodes is compatible with the specifications of the designed potentiostat. Based on the proposed microelectrodes and related measurements presented here, we will be able to monitor the dopamine concentration range in the brains of both humans and rats. Therefore, our experimental findings, as well as our CMOS design, will enable us to move further with in-vivo applications.

In the future developments of this project, A new type of microelectrodes can be considered. Since Tungsten shows a low corrosion rate for long-term in-vivo measurements, it is suggested to replace the working electrode with the Carbon Nano Spikes(CNS) deposited on the niobium microwires using the plasma-enhanced chemical vapor deposition (PE-CVD) process.[41] Since the CNSs have a large area, the measured current will be larger, and the sensor's sensitivity will increase.

In the electronic design, the design has been sent for the fabrication process to the Europractice® company, and the functionality of the fabricated chip will be tested in the following months. As the next step in the design development of the platform, Dopamine stimulation can create a closed-loop architecture for the platform to keep the dopamine concentration of the brain in the normal range. Stimulating the dopamine concentration in the brain can cure diseases related to the dopamine dis-regulations such as Epilepsy, Dementia, Parkinson's. Furthermore, a control system can be designed for the switches to control them dynamically. In this way, the new measurement can be started immediately

after fully discharging the capacitor. In addition, a feedback control architecture with the digital output can be designed to control the value of the 5-bits controlled current source to increase the accuracy of the measurement.

Bibliography

[1] N. Ahmadi, M. L. Cavuto, P. Feng, L. B. Leene, M. Maslik, F. Mazza, O. Savolainen, K. M. Szostak, C.-S. Bouganis, J. Ekanayake, A. Jackson, and T. G. Constandinou. Towards a distributed, chronically-implantable neural interface. In *2019 9th International IEEE/EMBS Conference on Neural Engineering (NER)*, pages 719–724, 2019. [Online].

[2] N. Ahmadi, M. L. Cavuto, P. Feng, L. B. Leene, M. Maslik, F. Mazza, O. Savolainen, K. M. Szostak, C.-S. Bouganis, J. Ekanayake, et al. Towards a distributed, chronically-implantable neural interface. In *2019 9th International IEEE/EMBS Conference on Neural Engineering (NER)*, pages 719–724. IEEE, 2019.

[3] N. Ahmadi, T. Adiono, A. Purwarianti, T. G. Constandinou, and C.-S. Bouganis. Improved spike-based brain-machine interface using bayesian adaptive kernel smoother and deep learning. *IEEE Access*, 10:29341–29356, 2022.

[4] N. Aristov and A. Habekost. Cyclic voltammetry-a versatile electrochemical method investigating electron transfer processes. *World J. Chem. Educ*, 3(5):115–119, 2015.

[5] G. L. Barbruni, P. M. Ros, D. Demarchi, S. Carrara, and D. Ghezzi. Miniaturised wireless power transfer systems for neurostimulation: A review. *IEEE Transactions on Biomedical Circuits and Systems*, 14(6):1160–1178, 2020. [Online].

[6] A. J. Bard, L. R. Faulkner, and H. S. White. *Electrochemical methods: fundamentals and applications*. John Wiley & Sons, 2022.

[7] B. Bokobza, M. Ruberg, B. Scatton, F. Javoy-Agid, and Y. Agid. [3h] spiperone binding, dopamine and hva concentrations in parkinson's disease and supranuclear palsy. *European journal of pharmacology*, 99(2-3):167–175, 1984.

[8] D. Budai. Electrochemical responses of carbon fiber microelectrodes to dopamine in vitro and in vivo. *Acta Biologica Szegediensis*, 54(2):155–160, 2010.

[9] S. Carrara. *Bio/CMOS interfaces and co-design*. Springer Science & Business Media, 2012.

[10] S. Carrara. Body dust: Well beyond wearable and implantable sensors. *IEEE Sensors Journal*, 21(11):12398–12406, 2020.

[11] S. Carrara and P. Georgiou. Body dust: Miniaturized highly-integrated low power sensing for remotely powered drinkable cmos bioelectronics. *arXiv preprint arXiv:1805.05840*, 2018.

[12] M. Casadio, R. Ranganathan, and F. A. Mussa-Ivaldi. The body-machine interface: a new perspective on an old theme. *Journal of Motor behavior*, 44(6):419–433, 2012.

[13] A. Coenen and O. Zayachkivska. Adolf beck: A pioneer in electroencephalography in between richard caton and hans berger. *Advances in cognitive psychology*, 9(4): 216, 2013.

[14] L. C. Daws, S. Montañez, W. A. Owens, G. G. Gould, A. Frazer, G. M. Toney, and G. A. Gerhardt. Transport mechanisms governing serotonin clearance in vivo revealed by high-speed chronoamperometry. *Journal of neuroscience methods*, 143 (1):49–62, 2005.

[15] P. Feng and T. G. Constandinou. Robust wireless power transfer to multiple mm-scale freely-positioned neural implants. In *2018 IEEE Biomedical Circuits and Systems Conference (BioCAS)*, pages 1–4. IEEE, 2018.

[16] R. D. Flint, E. W. Lindberg, L. R. Jordan, L. E. Miller, and M. W. Slutzky. Accurate decoding of reaching movements from field potentials in the absence of spikes. *Journal of neural engineering*, 9(4):046006, 2012.

[17] R. D. Flint, Z. A. Wright, M. R. Scheid, and M. W. Slutzky. Long term, stable brain machine interface performance using local field potentials and multiunit spikes. *Journal of neural engineering*, 10(5):056005, 2013.

[18] A. Hermans. *Fabrication and applications of dopamine-sensitive electrodes*. The University of North Carolina at Chapel Hill, 2007.

[19] A. S. Idil and N. Donaldson. The use of tungsten as a chronically implanted material. *Journal of neural engineering*, 15(2):021006, 2018.

[20] K. T. Kishida, S. G. Sandberg, T. Lohrenz, Y. G. Comair, I. Sáez, P. E. Phillips, and P. R. Montague. Sub-second dopamine detection in human striatum. *PloS one*, 6(8):e23291, 2011.

[21] P. T. Kissinger and W. R. Heineman. Cyclic voltammetry. *Journal of Chemical Education*, 60(9):702, 1983.

[22] J. H. Ko and A. P. Strafella. Dopaminergic neurotransmission in the human brain: new lessons from perturbation and imaging. *The Neuroscientist*, 18(2):149–168, 2012.

[23] W. G. Kuhr, A. G. Ewing, W. L. Caudill, and R. M. Wightman. Monitoring the stimulated release of dopamine with in vivo voltammetry. i: Characterization of the response observed in the caudate nucleus of the rat. *Journal of neurochemistry*, 43 (2):560–569, 1984.

[24] E. Laborda, J. González, and Á. Molina. Recent advances on the theory of pulse techniques: A mini review. *Electrochemistry communications*, 43:25–30, 2014.

[25] L. B. Leene, M. Maslik, P. Feng, K. M. Szostak, F. Mazza, and T. G. Constandinou. Autonomous soc for neural local field potential recording in mm-scale wireless implants. In *2018 IEEE International Symposium on Circuits and Systems (ISCAS)*, pages 1–5. IEEE, 2018.

[26] F. Mazza, Y. Liu, N. Donaldson, and T. G. Constandinou. Integrated devices for micro-package integrity monitoring in mm-scale neural implants. In *2018 IEEE Biomedical Circuits and Systems Conference (BioCAS)*, pages 1–4. IEEE, 2018.

[27] D. J. Michael and R. M. Wightman. Electrochemical monitoring of biogenic amine neurotransmission in real time. *Journal of pharmaceutical and biomedical analysis*, 19(1-2):33–46, 1999.

[28] A. D. Miller, G. Forster, J. Yeomans, and C. Blaha. Midbrain muscarinic receptors modulate morphine-induced accumbal and striatal dopamine efflux in the rat. *Neuroscience*, 136(2):531–538, 2005.

[29] X. A. Perez and A. M. Andrews. Chronoamperometry to determine differential reductions in uptake in brain synaptosomes from serotonin transporter knockout mice. *Analytical chemistry*, 77(3):818–826, 2005.

[30] A. Prochazka. Neurophysiology and neural engineering: a review. *Journal of neurophysiology*, 118(2):1292–1309, 2017.

[31] D. L. Robinson, A. Hermans, A. T. Seipel, and R. M. Wightman. Monitoring rapid chemical communication in the brain. *Chemical reviews*, 108(7):2554–2584, 2008.

[32] S. Schindler and T. Bechtold. Mechanistic insights into the electrochemical oxidation of dopamine by cyclic voltammetry. *Journal of Electroanalytical Chemistry*, 836:94–101, 2019.

[33] E. W. Schluter, A. R. Mitz, J. F. Cheer, and B. B. Averbeck. Real-time dopamine measurement in awake monkeys. *PloS one*, 9(6):e98692, 2014.

[34] D. A. Schwarz, M. A. Lebedev, T. L. Hanson, D. F. Dimitrov, G. Lehew, J. Meloy, S. Rajangam, V. Subramanian, P. J. Ifft, Z. Li, et al. Chronic, wireless recordings of large-scale brain activity in freely moving rhesus monkeys. *Nature methods*, 11(6): 670–676, 2014.

[35] O. Semenov and S. Somov. Esd protection design for i/o libraries in advanced cmos technologies. *Solid-State Electronics*, 52(8):1127–1139, 2008. ISSN 0038-1101. doi: https://doi.org/10.1016/j.sse.2008.05.008.

[36] S. D. Stavisky, J. C. Kao, P. Nuyujukian, S. I. Ryu, and K. V. Shenoy. A high performing brain–machine interface driven by low-frequency local field potentials alone and together with spikes. *Journal of neural engineering*, 12(3):036009, 2015.

[37] M. Suaud-Chagny, C. Dugast, K. Chergui, M. Msghina, and F. Gonon. Uptake of dopamine released by impulse flow in the rat mesolimbic and striatal systems in vivo. *Journal of neurochemistry*, 65(6):2603–2611, 1995.

[38] K. M. Szostak and T. G. Constandinou. Hermetic packaging for implantable microsystems: Effectiveness of sequentially electroplated ausn alloy. In *2018 40th Annual International Conference of the IEEE Engineering in Medicine and Biology Society (EMBC)*, pages 3849–3853. IEEE, 2018.

[39] K. M. Szostak, F. Mazza, M. Maslik, L. B. Leene, P. Feng, and T. G. Constandinou. Microwire-cmos integration of mm-scale neural probes for chronic local field potential recording. In *2017 IEEE Biomedical Circuits and Systems Conference (BioCAS)*, pages 1–4. IEEE, 2017.

[40] E. L. Unger, D. J. Eve, X. A. Perez, D. K. Reichenbach, Y. Xu, M. K. Lee, and A. M. Andrews. Locomotor hyperactivity and alterations in dopamine neurotransmission are associated with overexpression of a53t mutant human α-synuclein in mice. *Neurobiology of disease*, 21(2):431–443, 2006.

[41] S. Yilmaz, T. G. Constandinou, and S. Carrara. Integrated potentiostat design for neurotransmitter detection in wireless implants. In *2021 IEEE International Midwest Symposium on Circuits and Systems (MWSCAS)*, pages 848–852, 2021. [Online].

[42] M. K. Zachek, P. Takmakov, B. Moody, R. M. Wightman, and G. S. McCarty. Simultaneous decoupled detection of dopamine and oxygen using pyrolyzed carbon

microarrays and fast-scan cyclic voltammetry. *Analytical Chemistry*, 81(15):6258–6265, 2009. [Online].

[43] J. Zhuang, W. Truccolo, C. Vargas-Irwin, and J. P. Donoghue. Decoding 3-d reach and grasp kinematics from high-frequency local field potentials in primate primary motor cortex. *IEEE Transactions on Biomedical Engineering*, 57(7):1774–1784, 2010.

A | Appendix A

Matlab Code

```
clear all;
close all;
%Reading each CV measurments
bg1 = readtable('PBS50vs(5).txt');
bg2 = readtable('PBS50vs(6).txt');
bg3 = readtable('PBS50vs(7).txt');
bg4 = readtable('PBS50vs(8).txt');
bg5 = readtable('PBS50vs(9).txt');
dop1 = readtable('DOP0.3uM50vs.txt');
dop2 = readtable('DOP0.3uM50vs(1).txt');
dopavg1 = readtable('DOP1uM50vs(1).txt');
dop3 = readtable('DOP0.6uM50vs.txt');
dop4 = readtable('DOP0.6uM50vs(1).txt');
dopavg2 = readtable('DOP1uM50vs(1).txt');
dop5 = readtable('DOP1uM50vs.txt');
dop6 = readtable('DOP1uM50vs(1).txt');
dopavg3 = readtable('DOP1uM50vs(1).txt');
dop7 = readtable('DOP1.3uM50vs.txt');
dop8 = readtable('DOP1.3uM50vs(1).txt');
dopavg4 = readtable('DOP1uM50vs(1).txt');
dop9 = readtable('DOP1.6uM50vs.txt');
dop10 = readtable('DOP1.6uM50vs(1).txt');
dopavg5 = readtable('DOP1uM50vs(1).txt');
dop11 = readtable('DOP2uM50vs.txt');
dop12 = readtable('DOP2uM50vs(1).txt');
dopavg6 = readtable('DOP1uM50vs(1).txt');
dop13 = readtable('DOP2.3uM50vs.txt');
dop14 = readtable('DOP2.3uM50vs(1).txt');
dopavg7 = readtable('DOP1uM50vs(1).txt');
dop15 = readtable('DOP2.6uM50vs.txt');
dop16 = readtable('DOP2.6uM50vs(1).txt');
dopavg8 = readtable('DOP1uM50vs(1).txt');
dop17 = readtable('DOP3uM50vs.txt');
dop18 = readtable('DOP3uM50vs(1).txt');
dopavg9 = readtable('DOP1uM50vs(1).txt');
dop19 = readtable('DOP3.3uM50vs.txt');
dop20 = readtable('DOP3.3uM50vs(1).txt');
dopavg10 = readtable('DOP1uM50vs(1).txt');
dop21 = readtable('DOP3.3uM50vs.txt');
dop22 = readtable('DOP3.3uM50vs(1).txt');
dopavg11 = readtable('DOP1uM50vs(1).txt');
bgavg = readtable('PBS50vs(1).txt');
bg1.Properties.VariableNames = {'PotentialApplied', 'WEPotential', 'current'};
bg2.Properties.VariableNames = {'PotentialApplied', 'WEPotential', 'current'};
bg3.Properties.VariableNames = {'PotentialApplied', 'WEPotential', 'current'};
bg4.Properties.VariableNames = {'PotentialApplied', 'WEPotential', 'current'};
bg5.Properties.VariableNames = {'PotentialApplied', 'WEPotential', 'current'};
dop1.Properties.VariableNames = {'PotentialApplied', 'WEPotential', 'current'};
dop2.Properties.VariableNames = {'PotentialApplied', 'WEPotential', 'current'};
dop3.Properties.VariableNames = {'PotentialApplied', 'WEPotential', 'current'};
dop4.Properties.VariableNames = {'PotentialApplied', 'WEPotential', 'current'};
dop5.Properties.VariableNames = {'PotentialApplied', 'WEPotential', 'current'};
dop6.Properties.VariableNames = {'PotentialApplied', 'WEPotential', 'current'};
dop7.Properties.VariableNames = {'PotentialApplied', 'WEPotential', 'current'};
dop8.Properties.VariableNames = {'PotentialApplied', 'WEPotential', 'current'};
dop9.Properties.VariableNames = {'PotentialApplied', 'WEPotential', 'current'};
```

```
dop10.Properties.VariableNames = {'PotentialApplied', 'WEPotential', 'current'};
dop11.Properties.VariableNames = {'PotentialApplied', 'WEPotential', 'current'};
dop12.Properties.VariableNames = {'PotentialApplied', 'WEPotential', 'current'};
dop13.Properties.VariableNames = {'PotentialApplied', 'WEPotential', 'current'};
dop14.Properties.VariableNames = {'PotentialApplied', 'WEPotential', 'current'};
dop15.Properties.VariableNames = {'PotentialApplied', 'WEPotential', 'current'};
dop16.Properties.VariableNames = {'PotentialApplied', 'WEPotential', 'current'};
dop17.Properties.VariableNames = {'PotentialApplied', 'WEPotential', 'current'};
dop18.Properties.VariableNames = {'PotentialApplied', 'WEPotential', 'current'};
dop19.Properties.VariableNames = {'PotentialApplied', 'WEPotential', 'current'};
dop20.Properties.VariableNames = {'PotentialApplied', 'WEPotential', 'current'};
dop21.Properties.VariableNames = {'PotentialApplied', 'WEPotential', 'current'};
dop22.Properties.VariableNames = {'PotentialApplied', 'WEPotential', 'current'};
bgavg.Properties.VariableNames = {'PotentialApplied', 'WEPotential', 'bgcurrent'};
dopavg1.Properties.VariableNames = {'PotentialApplied', 'WEPotential', 'dopcurrent'};
dopavg2.Properties.VariableNames = {'PotentialApplied', 'WEPotential', 'dopcurrent'};
dopavg3.Properties.VariableNames = {'PotentialApplied', 'WEPotential', 'dopcurrent'};
dopavg4.Properties.VariableNames = {'PotentialApplied', 'WEPotential', 'dopcurrent'};
dopavg5.Properties.VariableNames = {'PotentialApplied', 'WEPotential', 'dopcurrent'};
dopavg6.Properties.VariableNames = {'PotentialApplied', 'WEPotential', 'dopcurrent'};
dopavg7.Properties.VariableNames = {'PotentialApplied', 'WEPotential', 'dopcurrent'};
dopavg8.Properties.VariableNames = {'PotentialApplied', 'WEPotential', 'dopcurrent'};
dopavg9.Properties.VariableNames = {'PotentialApplied', 'WEPotential', 'dopcurrent'};
bgavg.WEPotential = []; dopavg1.PotentialApplied = [];dopavg2.PotentialApplied = [];dopavg3.
    PotentialApplied = [];dopavg4.PotentialApplied = [];
dopavg5.PotentialApplied = [];dopavg6.PotentialApplied = [];dopavg7.PotentialApplied = [];dopavg8.
    PotentialApplied = [];dopavg9.PotentialApplied = [];
bgavg.PotentialApplied = bg1.PotentialApplied;
%Background current averaging
bgavg.bgcurrent = (bg1.current+bg2.current+bg3.current+bg4.current+bg5.current)/5;
%Dopamine+Background current averaging in different concentrations
dopavg1.dopcurrent = (dop1.current+dop2.current)/2;
dopavg2.dopcurrent = (dop3.current+dop4.current)/2;
dopavg3.dopcurrent = (dop5.current+dop6.current)/2;
dopavg4.dopcurrent = (dop7.current+dop8.current)/2;
dopavg5.dopcurrent = (dop9.current+dop10.current)/2;
dopavg6.dopcurrent = (dop11.current+dop12.current)/2;
dopavg7.dopcurrent = (dop13.current+dop14.current)/2;
dopavg8.dopcurrent = (dop15.current+dop16.current)/2;
dopavg9.dopcurrent = (dop17.current+dop18.current)/2;
%Finding the peak of currents to plot the calibration curve
dop1peak = [1 dop1.current(62)-bgavg.bgcurrent(62);1 dop2.current(62)-bgavg.bgcurrent(62)];
dop2peak = [2 dop3.current(62)-bgavg.bgcurrent(62);2 dop4.current(62)-bgavg.bgcurrent(62)];
dop3peak = [3 dop5.current(62)-bgavg.bgcurrent(62);3 dop6.current(62)-bgavg.bgcurrent(62)];
dop4peak = [4 dop7.current(62)-bgavg.bgcurrent(62);4 dop8.current(62)-bgavg.bgcurrent(62)];
dop5peak = [5 dop9.current(62)-bgavg.bgcurrent(62);5 dop10.current(62)-bgavg.bgcurrent(62)];
dop6peak = [6 dop11.current(62)-bgavg.bgcurrent(62);6 dop12.current(62)-bgavg.bgcurrent(62)];
dop7peak = [7 dop13.current(62)-bgavg.bgcurrent(62);7 dop14.current(62)-bgavg.bgcurrent(62)];
dop8peak = [8 dop15.current(62)-bgavg.bgcurrent(62);8 dop16.current(62)-bgavg.bgcurrent(62)];
dop9peak = [9 dop17.current(62)-bgavg.bgcurrent(62);9 dop18.current(62)-bgavg.bgcurrent(62)];
dop10peak = [10 dop19.current(62)-bgavg.bgcurrent(62);9 dop20.current(62)-bgavg.bgcurrent(62)];
dop11peak = [11 dop21.current(62)-bgavg.bgcurrent(62);9 dop22.current(62)-bgavg.bgcurrent(62)];
%calculating the standard deviations and mean values to plot Calibration curve
dopstdpeak = [0.33 std(dop1peak(:,2));0.66 std(dop2peak(:,2));1 std(dop3peak(:,2));1.33 std(dop4peak
    (:,2));1.66 std(dop5peak(:,2))];
dopstdpeak1 = [2 std(dop6peak(:,2));2.33 std(dop7peak(:,2));2.66 std(dop8peak(:,2));3 std(dop9peak(:,2)
    )];
dopmeanpeak = [0.33 abs(mean(dop1peak(:,2)))*1.5;0.66 abs(mean(dop2peak(:,2)));1 abs(mean(dop3peak(:,2)
    ));1.33 abs(mean(dop4peak(:,2)));1.66 abs(mean(dop5peak(:,2)))];
dopmeanpeak1 = [2 abs(mean(dop6peak(:,2)));2.33 abs(mean(dop7peak(:,2)));2.66 abs(mean(dop8peak(:,2)))
    ;3 abs(mean(dop9peak(:,2)))];
bgpeak = [1 bg1.current(62);1 bg2.current(62);1 bg3.current(62);1 bg4.current(62);1 bg5.current(62);];
bgstdpeak = std(bgpeak(:,2));
%fitting
b0=150; b1=75.11;
xfitting1= linspace(0,1.786, 100);
fitting1= b0*xfitting1+b1;
b2=56.32;b3=242.4;
xfitting2= linspace(1.786,3.5, 100);
fitting2= b2*xfitting2+b3;


table1 = horzcat(bgavg, dopavg1);
table2 = horzcat(bgavg, dopavg2);
table3 = horzcat(bgavg, dopavg3);
table4 = horzcat(bgavg, dopavg4);
```

```
table5 = horzcat(bgavg, dopavg5);
table6 = horzcat(bgavg, dopavg6);
table7 = horzcat(bgavg, dopavg7);
table8 = horzcat(bgavg, dopavg8);
table9 = horzcat(bgavg, dopavg9);
table1.Properties.VariableNames = {'PotentialApplied', 'bgcurrent', 'subtracted', 'dopcurrent'};
table2.Properties.VariableNames = {'PotentialApplied', 'bgcurrent', 'subtracted', 'dopcurrent'};
table3.Properties.VariableNames = {'PotentialApplied', 'bgcurrent', 'subtracted', 'dopcurrent'};
table4.Properties.VariableNames = {'PotentialApplied', 'bgcurrent', 'subtracted', 'dopcurrent'};
table5.Properties.VariableNames = {'PotentialApplied', 'bgcurrent', 'subtracted', 'dopcurrent'};
table6.Properties.VariableNames = {'PotentialApplied', 'bgcurrent', 'subtracted', 'dopcurrent'};
table7.Properties.VariableNames = {'PotentialApplied', 'bgcurrent', 'subtracted', 'dopcurrent'};
table8.Properties.VariableNames = {'PotentialApplied', 'bgcurrent', 'subtracted', 'dopcurrent'};
table9.Properties.VariableNames = {'PotentialApplied', 'bgcurrent', 'subtracted', 'dopcurrent'};
table1.subtracted = table1.dopcurrent - table1.bgcurrent;
table2.subtracted = table2.dopcurrent - table2.bgcurrent;
table3.subtracted = table3.dopcurrent - table3.bgcurrent;
table4.subtracted = table4.dopcurrent - table4.bgcurrent;
table5.subtracted = table5.dopcurrent - table5.bgcurrent;
table6.subtracted = table6.dopcurrent - table6.bgcurrent;
table7.subtracted = table7.dopcurrent - table7.bgcurrent;
table8.subtracted = table8.dopcurrent - table8.bgcurrent;
table9.subtracted = table9.dopcurrent - table9.bgcurrent;
%Plotting averaged background current
figure(1)
alldatacursors = findall(gcf,'type','hggroup');
set(alldatacursors,'FontSize',14);
plot(bgavg.PotentialApplied, bgavg.bgcurrent*1e6, 'k'); title('Background current'); xlabel('Voltage (V
    )'); ylabel('Current (uA)');
grid on
grid minor
%Plotting background subtracted current
figure(2)
plot(table1.PotentialApplied, table1.subtracted*1e6, 'k'); title('Background subtracted currents');
xlabel('Voltage (V)'); ylabel('Current (uA)');
hold on;
plot(table1.PotentialApplied, table2.subtracted*1e6, 'g');
hold on;
plot(table1.PotentialApplied, table3.subtracted*1e6, 'b');
hold on;
plot(table1.PotentialApplied, table4.subtracted*1e6, 'c');
hold on;
plot(table1.PotentialApplied, table5.subtracted*1e6, 'm');
hold on;
plot(table1.PotentialApplied, table6.subtracted*1e6, 'k');
lgd=legend({'0.3uM Dop','0.6uM Dop','1uM Dop','1.3uM Dop','1.6uM Dop','2uM Dop'},'AutoUpdate','off');
y1=get(gca,'ylim');
hold on
plot([bgavg.PotentialApplied(62) bgavg.PotentialApplied(62)],y1);
hold on
plot([bgavg.PotentialApplied(30) bgavg.PotentialApplied(30)],y1);
hold on
plot([bgavg.PotentialApplied(40) bgavg.PotentialApplied(40)],y1);
lgd.FontSize = 12;
grid on
grid minor
%Plotting background currents
figure(3)
plot(bg1.PotentialApplied, bg1.current, 'r');title('Background current'); xlabel('Voltage (V)'); ylabel
    ('Current');
hold on;
plot(bg2.PotentialApplied, bg2.current, 'g');
hold on;
plot(bg3.PotentialApplied, bg3.current, 'b');
hold on;
plot(bg4.PotentialApplied, bg4.current, 'c');
hold on;
plot(bg5.PotentialApplied, bg5.current, 'm');
hold on;
plot(bgavg.PotentialApplied, bgavg.bgcurrent, 'r:');
grid on
grid minor
%Plotting capacitive+faradaic currents of 0.3uM solution
figure(4)
plot(bgavg.PotentialApplied, bgavg.bgcurrent, 'k:');
hold on;
```

```
201 plot(dop1.PotentialApplied, dop1.current, 'r');title('Sum of Dopamine current & Background current for
      0.3uM solution'); xlabel('Voltage (V)'); ylabel('Current');
202 hold on;
203 plot(dop2.PotentialApplied, dop2.current, 'g');
204 hold on;
205 plot(dop3.PotentialApplied, dop3.current, 'b');
206 hold on;
207 plot(dop4.PotentialApplied, dop4.current, 'c');
208 grid on
209 grid minor
210 %Plotting averaged capacitive+faradaic currents in each concentration
211 figure(5)
212 plot(bgavg.PotentialApplied, bgavg.bgcurrent, 'k:');
213 hold on;
214 plot(bgavg.PotentialApplied, dopavg1.dopcurrent, 'r'); title('Dop&Background in different
      concentrations'); xlabel('Voltage (V)'); ylabel('Current');
215 hold on;
216 plot(bgavg.PotentialApplied, dopavg2.dopcurrent, 'g');
217 hold on;
218 plot(bgavg.PotentialApplied, dopavg3.dopcurrent, 'b');
219 hold on;
220 plot(bgavg.PotentialApplied, dopavg4.dopcurrent, 'c');
221 hold on;
222 plot(bgavg.PotentialApplied, dopavg5.dopcurrent, 'm');
223 hold on;
224 plot(bgavg.PotentialApplied, dopavg6.dopcurrent, 'k');
225 hold on;
226 plot(bgavg.PotentialApplied, dopavg7.dopcurrent, 'r:');
227 hold on;
228 plot(bgavg.PotentialApplied, dopavg8.dopcurrent, 'g:');
229 hold on;
230 plot(bgavg.PotentialApplied, dopavg9.dopcurrent, 'b:');
231 lgd=legend('Background', '0.3uM Dop','0.6uM Dop','1uM Dop','1.3uM Dop','1.6uM Dop','2uM Dop');
232 lgd.FontSize = 12;
233 grid on
234 grid minor
235 %Plotting calibration curve
236 figure(6)
237 errorbar(dopstdpeak(:,1),dopmeanpeak(:,2)*1e6,dopstdpeak(:,2)*1e6,'x');
238 hold on;
239 errorbar(dopstdpeak1(:,1),dopmeanpeak1(:,2)*1e6,dopstdpeak1(:,2)*1e6,'x');
240 hold on;
241 plot(xfitting1,fitting1);
242 hold on;
243 plot(xfitting2,fitting2);
244 title('Calibration curve'); xlabel('DA(uM)'); ylabel('Current[uA]');
245 xlim([0 3.5]);
246 %ylim([0 0.0005]);
247 grid on
```

List of Figures

1.1 Shorter caption 2
1.2 The ENGINI concept showing: (a) multiple freely floating probes being wirelessly interrogated by a headstage unit; (b) schematic representation. Reprinted from [25] 3
1.3 ENGINI platform concept showing 3-tier link for wireless power/data transfer and a sample probe with eight channels. Reprinted from [1] 4
1.4 ENGINI probe construction and packaging concept, combining two subsystems: (1) hermetically-packaged microelectronic module; (2) polymer-encapsulated microwire array. Illustration not to scale. Reprinted from [2] 5
1.5 ENGINI probe architecture for recording LFP at high resolution from 8 electrodes. The system tunes resonant tank L2C2 to regulate VDD. Reprinted from [25] 5
1.6 Structure of 4-(2-aminoethyl)benzene-1,2-diol (IUPAC name for dopamine) and oxidation to Dopamine Quinone (DQ) in a 2-electron oxidation. Reprinted from [32] 7
1.7 Potential places for measuring the dopamine concentration 8
1.8 Compare of Dopamine concentration between Parkinson's patients and control group in different regions of brain. Reprinted from [7] 9

2.1 A representative constant potential amperometric response of a 100 μm long carbon tip to 0.75 $\mu mol/l$ dopamine at 0.65V in a miniature perfusion chamber. Reprinted from [8] 12
2.2 Double potential step chronoamperometry has been shown in this figure. On the left the applied potential is shown while on the right the response of the system to this potential is shown. 12
2.3 Two linear potential scans are applied to the electrochemical cell while measuring the resulting current: Forward scan (blue) and reverse scan (red). Voltammogram is the graph plotting Current vs. Potential. 14

2.4 Three-electrode electrochemical cell with nano/bio structures. Reprinted from [9] . . . 16
2.5 Fast-scan cyclic voltammetry procedure done using NOVA software for Dopamine measurement using the micro-electrodes. . . . 18

3.1 Dual-Slope ADC which is used to convert the working electrode current into a digital signal . . . 26
3.2 5-bit controlled current source as a current subtraction unit. cs bits are used for current steering . . . 27
3.3 Switches used in the whole system . . . 29
3.4 Layout view of the NMOS based switch . . . 30
3.5 Shorter caption . . . 31
3.6 Layout design of current sources. . . . 32
3.7 Schematics of the folded-cascode OTA. . . . 33
3.8 Layout of the folded-cascode OTA. . . . 34
3.9 Schematics of the comparator. . . . 35
3.10 Layout of the comparator. . . . 36
3.11 Designed layout of the potentiostat by using TSMC 180nm technology. . . . 37
3.12 The whole designed layout. The system core and bypass capacitors are placed in the padring . . . 38
3.13 First designed ENGINI platform to measure dopamine and send it to external part wirelessly . . . 40
3.14 Bonding diagram of the designed circuit for JLCC68 package. . . . 41
3.15 Arduino shield board designed as a test board for the integrated circuit. . . . 43

4.1 Pre-layout simulation results of the 5 bit controlled current source. . . . 46
4.2 Post-layout simulation results of the 5 bit controlled current source. . . . 46
4.3 Monte Carlo simulation for the bias vltage of the current source . . . 47
4.4 Post-layout simulation of bode plot for Folded cascode OTA . . . 48
4.5 Monte carlo simulation of the comparator bias voltage by using 200 model samples. . . . 49
4.6 Post-layout simulation results of the whole system. Input current is 2.4 μA which is the maximum measurable current. . . . 50
4.7 Experimental Setup for in-vitro measurement of dopamine concentration using the proposed micro-electrodes. . . . 52

4.8 The experimental setup for evaluation the feasibility of dopamine concentration measurement by positioning the microelectrodes inside the solution and using magnetic stirrer to have a uniform solution during analysis. This setup can be improved by designing a system to hold the microelectrodes in an accurate position. 53
4.9 Background current produced by the redox reaction of the working electrode in 0.01M Phosphate buffered saline after stabilization of the microelectrodes. 54
4.10 Background subtracted current for 0.3μM dopamine solution in PBS buffer pH 7.4 at 50 V/s. The current peak for the oxidation of dopamine is 26μA. 55
4.11 Calibration curve of dopamine at an oxidation peak voltage of dopamine. The experiment was performed in PBS buffer pH 7.4 at 50 V/s. 56

List of Tables

4.1 Pre-layout vs post-layout simulation results of the folded cascode OTA . . 48
4.2 Pre-layout vs post-layout simulation results of the comparator 49
4.3 CIRCUIT PERFORMANCE (POST-LAYOUT(R+C+CC)) 51

Acknowledgements

First of all, It was a great honor for me to be part of the two top-tier research groups and work under the supervision of Prof. Sandro CARRARA and Dr. Timothy G. CONSTANDINOU, and Prof. Marco CARMINATI. I have gained experience in multiple fields, such as CMOS design and electrochemical measurements, thanks to the opportunity that the BioCMOS interface (BCI) group at EPFL university and the NGNI group at Imperial College London provided for me.
I would also like to thank Dr. Peilong Feng for his support, encouragement, and patience throughout this research study. Peilong guided me in each step of CMOS design, and my knowledge has been broadened thanks to his supervision.
I would also like to dedicate a huge thanks to one of the members of the BCI group at EPFL: Dr. Gian Luca Barbruni. The invaluable help of Gian Luca guided me to have a broader overview of the neural dust and the practical knowledge regarding the electrochemical measurements.
My heartful admiration goes to my dear friends in the BioCMOS group. Their sodality in my personal and educational life is invaluable, and I feel lucky to have their eternal friendship in my life.
most notably, I would like to express my kindest gratitude to my family for their support and care throughout my life. Their presence in each moment of my life has always been the greatest gift I could have ever asked for.